2D-NANOLATTICES

FP7-ICT-2009-C (FET Open)

Highly anisotropic graphite-like emiconductor/dielectric 2D nanolattices

Deliverable D1.5

Anisotropic electronic properties and the effect of strain in Si/Ge-based superlattices

Report prepared by Augustin Lu Ahn-Koa and Geoffrey Pourtois, Imec Leuven

Contributors: imec

Preparation Date: June 21st, 2013

Report version number: final

Classification: Public

Contract Start Date: 01/06/2011

Duration: 36 months

Project Coordinator: NCSR- D (*Dr. A. Dimoulas*)

Contractors: IMEC, KULeuven, CNR, CNRS, U. Marseille

Project funded by the European Community under the "Future and Emerging Technologies" Programme

D1.5 Participant	MM/planned	MM/actual	Justification of deviation
IMEC (Lead)	7	3	The planned MM were not initially declared right

1 Modeling of the atomic and electronic structures of the Si(Ge)/O(C,N) superlattices (Imec)

1.1 Introduction

Deliverable 1.5 aims at studying the anisotropic electronic properties and the effects of strain in Si/Ge-based superlattices using atomistic modeling techniques. In this report, we discuss the electronic and structural properties of Si(Ge)/O(C,N) superlattices, as currently investigated experimentally in WP2, Task 2.6. Using reactive molecular dynamics simulations, we modeled the impact of temperature and of the substrate orientation on the diffusion and on the reaction of oxygen and nitrogen on Si (100), Si(110) and Si(111) substrates. Based on the topologies found, we built a set of representative models of Si/O(N) superlattices and studied their structural and electronic properties (band structure, band gap, effective masses). Given that the growth mechanisms of C on Si substrates are already well reported in literature, we limited ourselves to the study of structural and electronic properties of ideal Si/C superlattices built through a simple chemical substitution of the Si(Ge) sites by C in bulk Si. The Ge superlattice homologs have been built by trivially substituting Si by Ge in the models.

1.2 Methodology

The growth of the oxygen/nitrogen monolayers on a silicon substrate to build superlatices has been simulated by using reactive classical molecular dynamic simulations based on the Reactive Force Field (ReaxFF) (for oxygen) {1} and on the Tersoff many-body potentials (for nitrogen {2}). The ReaxFF potential uses the concept of partial bond orders to accurately model bond breaking and bond formation, and is based on the bond length – bond order / bond order – bond energy relationship introduced by Abell {3}. Previous studies indicated that this approach accurately describes bond breaking and formation, as well as the expansion of the Si crystal during oxide formation process (see for instance reference {4}). Unfortunately, the parameterization present for nitrogen in ReaxFF is not robust enough to describe correctly the nitridation mechanisms of silicon. As an alternative, we used the many-body potential developed by Tersoff combined with the parametrization proposed by de Brito Mota et al {5}. This technique has been reported to be able to correctly capture the stability of different crystalline phases of silicon nitride together with the distribution characteristic of the coordination shell for Si and N in different amorphous phases {5}.

The ozone and nitridation treatments of the surfaces have been modeled assuming a spontaneous decomposition of the molecules with the substrate, using hence either atomic oxygen or atomic nitrogen as a reactive species. For the thermal oxidation process, we also considered molecular oxygen. Different slab models representative of the Si(100){2x1}, Si(110) and Si(111) (Figure 1) reconstructed surfaces have been built. The latter are made of 15 monolayers of silicon and are coupled with periodic boundary conditions along the X and Y directions. A reflective periodic boundary condition has been set perpendicular to the surface, while the other directions are periodic. To mimic the bulk behavior of silicon, the bottom two layers of the slab were kept fixed. During the reaction process, the surfaces have been oxidized by the successive collisions of oxygen molecules/atoms at 298, 498 and 698 K

to account for a thermal oxidation and an ozone treatment. The resulting structures have been subsequently equilibrated using the Bussi heat bath (NVE dynamics) {6} for 10 ps with a damping constant of 5 (pressure damping constant) and 0.01 (temperature damping constant) ps. An integration time step of 0.5 fs has been used to integrate the Newton equations of movement.

The oxidation/nitridation processes have been described by the introduction of a fixed number of oxygen/nitrogen atoms and molecules that are randomly distributed and orientated into the upper space of the silicon buffer to bombard it. Upon reaction with the surface, a new reactive molecule/atom is automatically added such that the total partial pressure is maintained constant throughout the dynamics. To complete the picture, we also considered the case of the addition of a new molecule every 10^4 fs, independently of its reaction with the substrate. In this scenario, the partial pressure is allowed to vary through time.

Given that chemical reactions are 'rare' events at the femtosecond time scale, the pressure has been artificially maintained to be minimum 600 bar in order to maximize the number of collisions with the substrate and hence to maintain the computational efforts tractable within the scope of this project. We ran $2x10^7$ numerical iterations per simulation, which corresponds to the monitoring of the dynamics of the system for 10 ns.

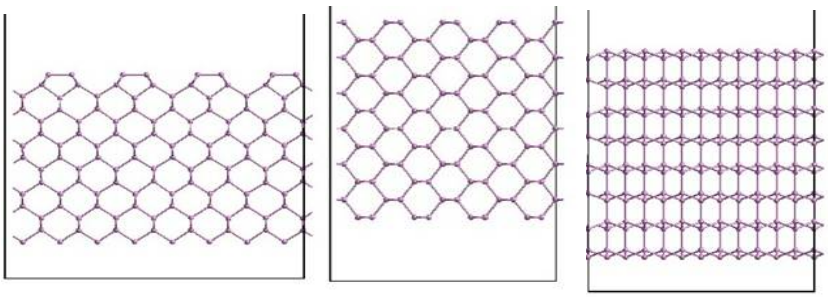

Figure 1: Illustrations of the 2x1 (100) (left), (110) (middle) and (111) (right) surface reconstructions used during the molecular dynamics simulations.

Most of the first-principles density functional theory (DFT) simulations have been performed using the quantum espresso package {7}, based on the generalized gradient approximation exchange correlation functional developed by Perdew-Burke-Ernzerhof {8}. This approach has been proven to offer quantitative insights in terms of ground state lattice parameters and a qualitative description of the electronic properties. Indeed, DFT suffers from a pathological underestimation of the electronic gap due to a poor description of non-local correlation effects and of the self-interaction. As a result, the computed band gap of bulk silicon and germanium are predicted to be 0.6 and 0 eV, instead of 1.2 and 0.66 eV, respectively. To alleviate this severe underestimation, we used the HSE {9} hybrid exchange correlation functional as proposed by Alkauskas et al {10} and the exchange correlation functional proposed by Tran and Blaha {11}. These two approaches have been shown to provide evaluations of the band gaps within a few percents of the experimental values {10-11}. The screening factor used to control the screening of the Hartree-Fock exchange for the silicon based systems are 0.11 in the hybrid functional. Convergence of the kinetic energy and of the

integration of the Brillouin zone has been ensured true thorough numerical tests and have been found to be 10^{-3} eV/atom. Note that given the fact that these two functionals are computationally very demanding, we used for the computation of the band structure and for the effective masses a lower cost approach, i.e. the PBE and the PBE+U functionals {12} for the silicon and germanium systems, respectively. For Ge, the U value (5 eV) has been fitted to reproduce the results generated by the functional developed by Tran and Blaha.

1.3 Results

1.3.1 Oxygen based superlattices

Keeping in mind that we target growing a (sub-)monolayer of silicon/germanium sub-oxide/nitride epitaxially on silicon/germanium to tune the band structure without building a quantum well, we have been investigating the impact of temperature on the reactivity of oxygen/nitrogen. Ideally, the grown perturbing layer should be uniform in terms of thickness and atomic coordination, and the diffusion of the interspersing species should be limited to the very first atomic layers of the semiconductor, saturating all the surface dangling bonds, without altering the topology of the underlying crystal. For instance, for the {2x1} (100) reconstructed surface, the two dangling bonds pointing out of the surface dimers should be saturated with the absorbed species. Also, oxygen/nitrogen should be 'flexible' enough to accommodate the substrate topology/coordination to allow silicon/germanium to be further grown epitaxially. It is also very likely that due to the electron transfer that goes hand to hand with the formation of chemical bonds, the surface reconstruction will be perturbed, ending to the breaking the silicon dimer and to the generation of additional surface dangling bonds to be saturated (as suggested by references {13-15}). As a result, we target controlling the surface reaction with silicon/germanium such that the surface/crystal structure is saturated and quasi-unperturbed. This suggests, in the case of oxygen, that silicon should be in majority in oxidation stage one or two (i.e. bonded once or twice with oxygen). Higher oxidation degrees would imply losing the symmetry of the silicon crystal which would lead to the growth of an amorphous SiOx/GeOx.

To evaluate if such a control is possible, we monitored the evolution of the silicon oxidation for 10ns for a set of thermal treatments spanning from 298 to 698 K (Figure 3). Experimentally, the time window of the oxidation process ranges from seconds to hours, which cannot be captured through our simulations. However, a large oxygen partial pressure help boosting the kinetics observed and probing larger time scales of the reaction (see below).

At room temperature (Figure 3), the oxidation quickly saturates and reaches a plateau with 1 monolayer (ML) of silicon atoms in oxidation stage 1 (Si+1) and ~ 0.5 ML of Si+2. No trace of Si+3 and Si+4 is observed within the studied time windows. This indicates that the kinetic of formation of a high oxidation stage in silicon is slower than for a low one. As expected, increasing the temperature to 498K (Figure 3) roughly maintains the concentration of Si+1 to ~ 1ML, while it favors the formation of Si+2 (~ 1ML) and Si+3 (~0.5 ML), respectively. A few percent of silicon in its +4 oxidation stage is also found. Counter intuitively, a further increases of the temperature leads to a seemingly gradual enhancement of the population of the Si+1 (Figure 3-698K). Given that the dynamics are monitored for a constant time window

and that the thermal variations impact on the degree of advancement of the kinetics, it is difficult to compare directly the different temperatures. Consequently, we converted the time steps of the dynamics into the number of particles that react with the surface per time unit (i.e. into a fluence metrics) that reflects more accurately the progression of the reaction (Figure 4). Also, to gain further insights into the observed behavior, we divided the silicon slabs into different regions/layers, each containing 4 monolayers (5 Å) of silicon. The position of the first slab is referenced as being the top of the reconstructed and unoxidized silicon surface (see Figure 2).

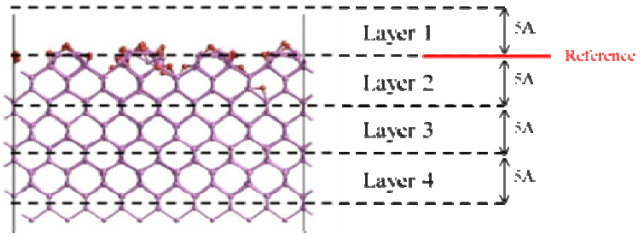

Figure 2: Schematic illustration of the partitioning used to monitor the distribution of oxygen and the oxidation stage of silicon during the molecular dynamics simulations. The silicon and oxygen atoms are depicted in pink and red, respectively.

At 298K, the oxygen diffusion and its reaction with silicon are mainly cantoned within the first 5 Å of the silicon slab (Figure 4); confining the Si+1 and Si+2 in this region. Raising the temperature to 698K, enhances the diffusion of oxygen deeper into the substrate (up to ~ 1nm). This is translated by an increase of the Si+1 population in the slab between 0.5 to 1nm. The increase in thermal energy also favors the oxidation process and promotes the formation of Si+2 and Si+3 close to the surface (0 to -0.5 nm) and the expansion of SiO_2 (0.5nm to 0nm). The formation of Si+3 is accompanied with a reduction of the concentration of Si+1 in this region (not shown).

In order to gain further insights into the reactions of oxidation, we enhanced the probability of collision of molecular oxygen with the substrate by adding a new molecule of oxygen every 10^4 femtoseconds, while maintaining the temperature constant. In this situation, the oxygen partial pressure is allowed to increase/decrease through time. As illustrated in Figure 8, for 298 and 498 K, this results into an improved probability of collision with the substrate and shifts the time window monitored by the dynamics. As a result, the fluence probed by the dynamics is multiplied by 4 and 2 at 298 and 498 K, respectively with respect to the “constant pressure” cases (Figure 4).

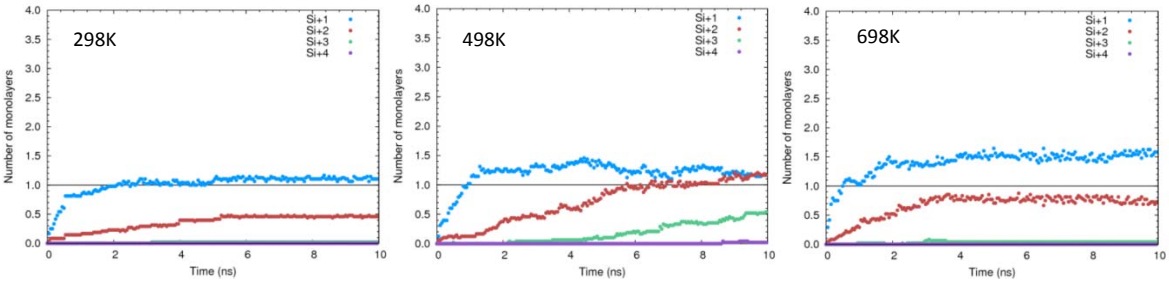

Figure 3: Evolution of the oxidation of Si(100) computed at 298, 498 and 698 K in contact with molecular oxygen at constant pressure. The dotted line corresponds to the 1 monolayer of oxygen reacting with the substrate. The contribution of Si+1, Si+2, Si+3 and Si+4 are colored in blue, red, green and purple, respectively.

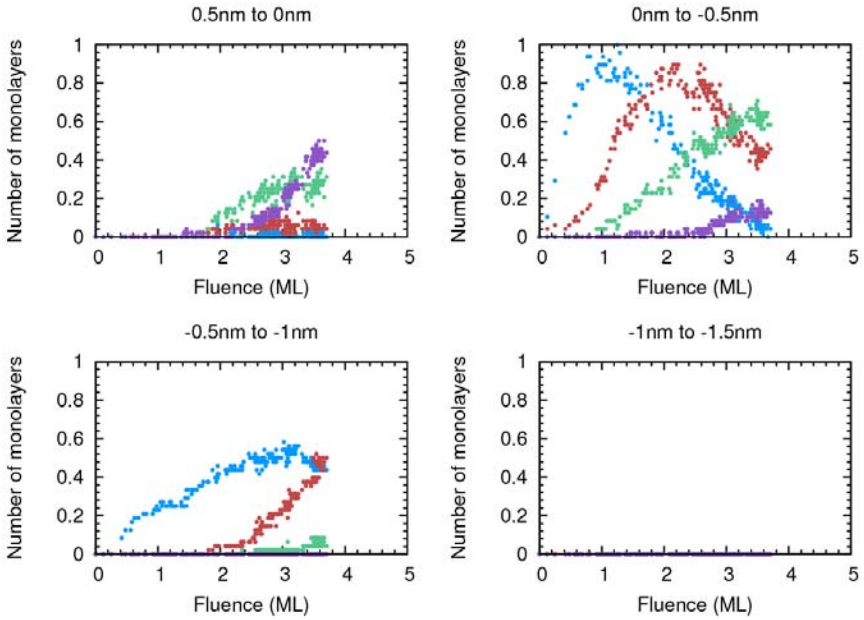

Figure 4: Evolution of the oxidation process with respect to the oxygen fluence, projected per silicon layer for the Si(100) case at 298K. The ordinate is normalized with respect to the number of atoms required to form 1ML of oxygen sandwiched with silicon. The contribution of Si+1, Si+2, Si+3 and Si+4 are colored in blue, red, green and purple, respectively.

Similarly to the "constant pressure" model, we observed the predominance of Si+1 species at low fluence. Indeed, in the earliest stage, the absorbed oxygen atoms bind themselves according to one of the bond configurations shown in Figure 5. Consistently with previous findings {13-15}, we find that back-bond (B), dimer-bridge(D), on-dimer (D1), peroxyl (O) and on-top (T) configurations are present (Figure 5) on the {2x1} Si(100) surface. The D configuration is found as soon as the first subsurface layer becomes oxidized and the peroxyl (O) gets rapidly unstable. The Si+2 peak indicates the apparition of two bonds, that are typically of the BB, DB, BT or BD1 types, of which the BB and BD1 ones dominate. As the oxidation proceeds, the Si+1 peak is gradually reduced while the Si+2 and Si+3 ones grow to coexist. As from a fluence of 3ML, the signature of Si+4 gradually appears on top of the oxidized surface. As for the ‘constant pressure’ case, increasing the temperature leads to an enhanced diffusion of oxygen into the substrate and to a boosted kinetic of reaction. To

further extend the time scale windows monitored, while maintaining the computational time tractable, we artificially increased the kinetic energy of the impeding molecules from ~0.06 eV (the kinetic energy generated at 698K) to 3eV, while maintaining the temperature of the thermostat at 298K. These conditions correspond to a plasma induced oxidation at room temperature. Figure 6 shows that the distribution obtained is qualitatively similar to the one generated through the thermal oxidation process, with a dominance of Si+1 species at low fluence.

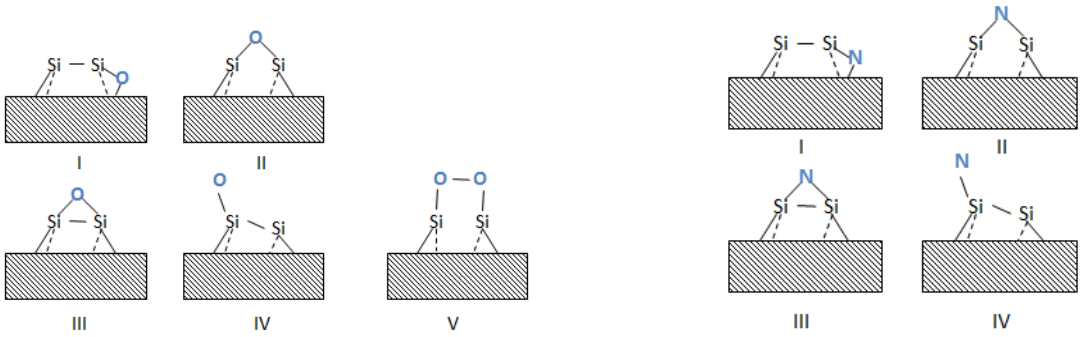

Figure 5: Bonding configurations observed for an oxygen (left)/nitrogen (right) atom in contact with a Si(100){2x1} surface in the initial silicon oxidation: (I) back-bond (B), (II) dimer-bridge (D), (III) on-dimer (D1), (IV) on-top (T) and (V) (O) peroxyl structures.

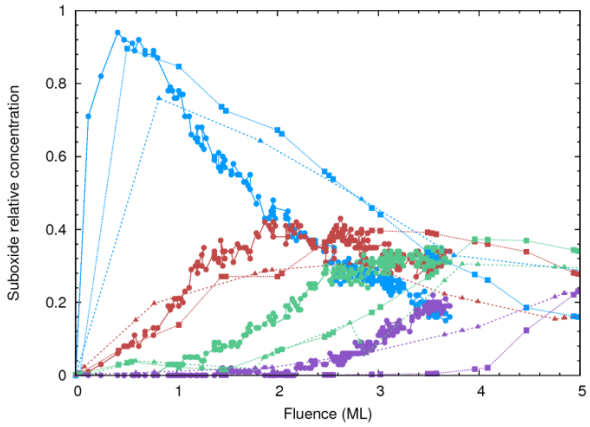

Figure 6: Evolution of the oxidation of Si(100) computed using a room temperature plasma oxidation process for molecular (kinetic energy of the molecule: 3eV - dashed line with closed triangles), atomic oxygen (energy of the molecule 3eV – dotted line with filled squares) and thermal oxidation (0.06 eV – continuous line with filled circles). The contribution of Si+1, Si+2, Si+3 and Si+4 are colored in blue, red, green and purple, respectively.

The latter species are gradually consumed during the oxidation process and converted into Si+2, Si+3 and later, into Si+4 through the growth of amorphous SiO_2. The dominance of Si+1 at low fluence is also found to occur for the exposition to atomic oxygen. The occurrence of Si+2 and Si+3 occur at lower fluences for a thermal oxidation process than for a plasma one. As a last point, thermal oxidation promotes a lower penetration of the oxygen into the silicon surface upon bombardment than with plasma conditions, which suggests a better controllability of the thickness of the grown interspersing species.

Consistently, these different oxidation conditions point towards the fact at low fluence, Si+1 is a predominant oxidation state at the surface. The composition of the peaks and their distribution for fluences lower than 1ML suggest that a thermal oxidation process using molecular oxygen maximizes the number of Si+1 sites generated at the silicon surface. This trend remains true whenever the orientation of the silicon substrate is changed, going for instance from (100) to (110) and (111) (Figure 8). The role of the substrate orientation, and hence of the topology/atomic density, are translated by a slightly higher population of Si+1 for Si(100) than for the other surfaces. Beyond a fluence of 2 ML, Si(111) has a larger fraction of Si+2 into the layers. For Si(110), Si+3 appears at a lower fluence compared to the other surfaces (Figure 9). Finally, we also gauged the impact of hydrogenation of a silicon surface on the oxidation process by considering the case of the oxidation of hydrogenated Si(111) (Figure 8). At low temperatures (298-498K), the presence of hydrogen leads to a 'delay' in the oxidation process. It requires several collisions with the surface for the impacting oxygen molecules to react with hydrogen to form water (Figure 8). Once one or several sites are dehydrogenated, they act as weak spots for oxygen to penetrate into the substrate. As a result, traces of Si+2, Si+3 and Si+4 are detected at lower fluences than with respect to the non-hydrogenated (111) case. This also leads to a less uniform oxidation of the surface. A higher thermal treatment (698 K) promotes the desorption of hydrogen from the surface and leads to an oxidation profile similar to the Si(111) case. In summary, our results suggest that the combination of dehydrogenated {2x1} Si(100), oxidized with molecular oxygen, at low temperature offers the most promising conditions to build Si-O superlattices.

Starting from the hypothesis that Si+1 is the dominating oxidation state at the Si(100) surface and using the topologies reported in Figure 5, we built a set of representative models of an epitaxial superlattice (Figure 7). In this configuration, oxygen is inserted interstitially in a Si-Si bond. Si hence adopts a coordination 4 with a +1 oxidation stage in the crystal lattice. The position of the Si atoms is maintained to be close to the bulk Si one. Each silicon in contact with the oxygen plane adopts an epoxy like configuration (model II – Figure 5). The structure has been built to accommodate a concentration of maximum ~$1.4x10^{15}$ (0.5ML) oxygen/cm^2 (1ML) (Figure 7). We refer this model as being SixOy_1, where x and y correspond to the number of monolayers used. We also built an alternative structure in which silicon adopts exclusively a +2 oxidation stage to determine the impact of a different oxidation state on the electronic properties of the stack (labeled as SixOy_2). In this topology, each silicon atom is surrounded by two oxygen ones along the (001) plane (Figure 7). This leads to an oxygen atomic concentration of interspersing species up to ~$3x10^{15}$ atom/cm^2 (1ML) (Figure 7).

(SixOy_1) (SixOy_2)

Figure 7: Illustration of Si/SiOx superlattices built using 3ML of Si and 0.5ML(SixOy_1)/1ML (SixOy_2) of oxygen. The silicon and oxygen atoms are depicted in pink and red, respectively.

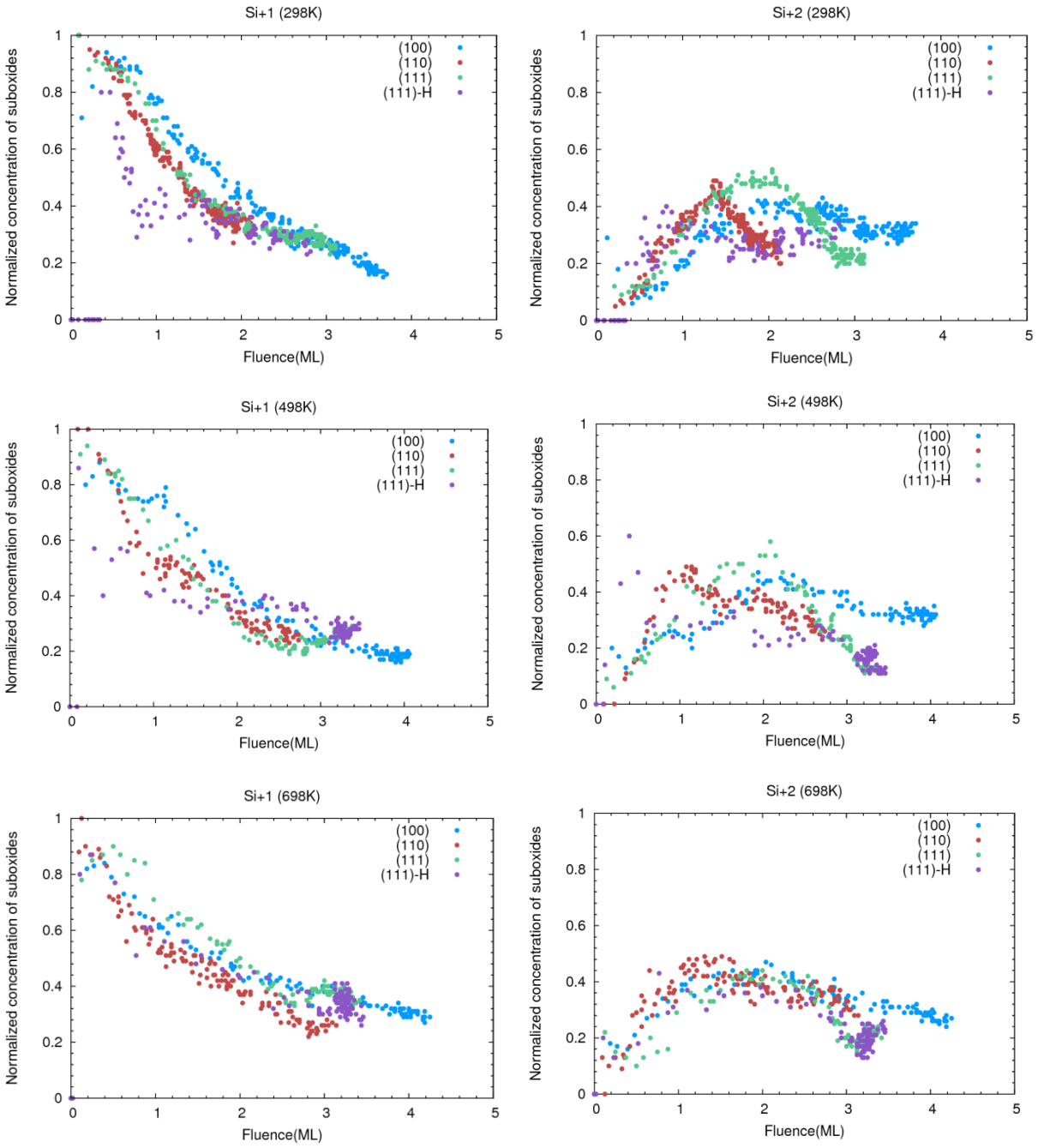

Figure 8: Comparison of the evolution of the oxidation process with respect to the fluence computed on {2x1} Si(100), Si(110) and Si(111) using molecular oxygen at 298, 498 and 698K for Si+1 and Si+2. (111-H) denotes an hydrogenated silicon (111) surface.

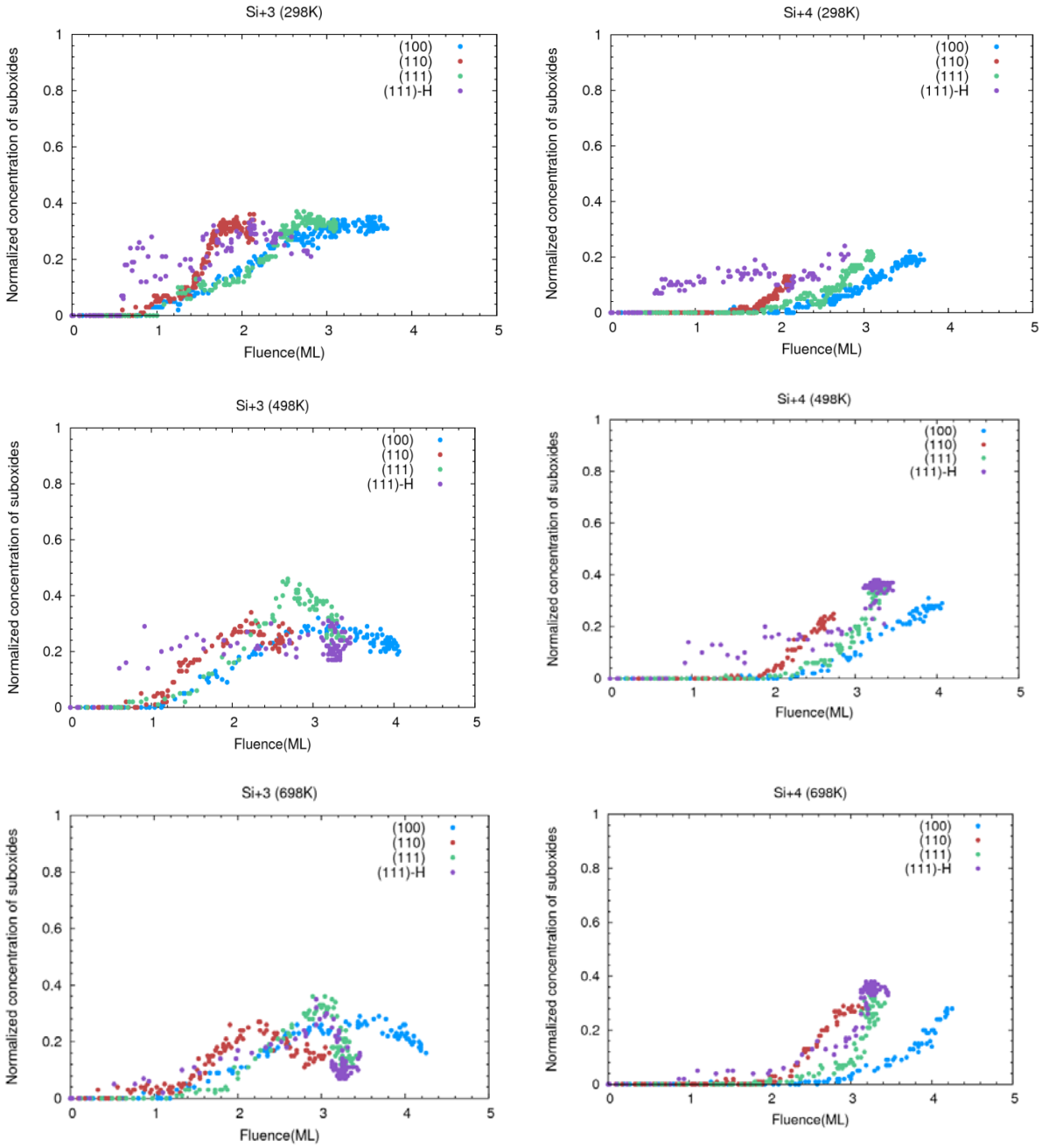

Figure 9: Comparison of the evolution of the oxidation process with respect to the fluence computed on 2x1 Si(100), Si(110) and Si(111) using molecular oxygen at 298, 498 and 698K for Si+3 and Si+4. (111-H) denotes an hydrogenated silicon (111) surface.

For the sake of simplicity, we limited ourselves to symmetric superlattices and to a number of silicon monolayers spanning from 3 [4] to 7 [6-8] ones for the SixOy_2 [SixOy_1] structures. The introduction of oxygen induces a perturbation into the lattice parameters with respect to the silicon bulk case (Figure 18). Indeed, the Si-O bond (1.67 Å) being shorter than the Si-Si one (2.35 Å) by about ~ 28 %, they lead to a contraction of the lattice constant. As a result, the number of oxygen introduced, in other words the oxidation stage of the superlattice,

determines the lattice constant of the system and hence also the possibility to grow them epitaxialy. As a rule of thumb, silicon can be strained up to maximum 4% before undergoing a strain relaxation process that generates misfit dislocations in its network, as reported for epitaxial silicon on germanium {16}. According to the changes in the lattice parameters with respect to bulk Si, the superlattices of the SixOy_1 type (Figure 18) could sustain the presence of up to maximum ~6 ML of sandwiched silicon per unit cell before reaching the critical threshold that would lead to a relaxation of the stress built into the layer. For the SixOy_2 case, the large compressibility induced along the (001) direction by the Si+2 oxidation state leads to the accumulation of high strain, even for silicon layers as thin as 3ML. This indicates that if a Si+2 configuration is chosen as a growth template, the deposited layers will relax themselves through either a lattice dislocation process or through an amorphization such that the built-in stress is minimized. Note that the topologies that we propose are similar to the ones suggested by Mears et al {17}, and Tsu et al {18}. According to the strain based considerations, only the SixOy_1 configurations would allow the growth of epitaxial superlattices.

To gain some insights into the electronic properties of these stacks, we computed the band structures of the SixOy_1 and SixOy_2 models (Figure 13). At this stage, we have to face a technical difficulty bound to the folding of the bands in the Brillouin zone. Indeed, the ratio of oxygen and silicon used in our models forces us to build relatively large supercell, i.e. non primitive, models. A direct consequence of the use of non-primitive unit cell is the folding of the bands, due to the reduction of the dimensions of the Brillouin zone. This leads to the overlap and to the shifts of bands through the Brillouin zone and makes the analysis of the electronic properties (and hence of the effective masses) complex. To alleviate this problem, we implemented the technique proposed by Haverkort et al {19}. The approach consists into computing a weight ($I_{b,k}^{\tau,\tau'}$) for each eigenvalue of the band structure, based on a Fourier transform of the projected atomic coefficient/contribution ($C_{b,t,k}^{\tau}$) of the wavefunction on an orbital of site (r_i). This weight (Eq.1.) represents the contribution of the electronic state into the reduced primitive Brillouin zone. A ‘0’ value implies a cancelation of the electronic state as illustrated for the case of the 3x3 silicon supercell in Figure 11 and allows us reconstructing the original band structure of bulk silicon (Figure 11).

$$I_{b,k}^{\tau,\tau'} = \frac{1}{N_i}\left(\sum_i e^{-tk.r_i} C_{b,t,k}^{\tau'}\right) * \left(\sum_i e^{-tk.r_i} C_{b,t,k}^{\tau}\right) \qquad \text{Eq. 1}$$

We hence investigated the evolution of the electronic properties of the SixOy_1 and SixOy_2 models. As expected, the inclusion of the oxygen 1/0.5 ML leads to the perturbation of the band structure of silicon (Figures 10 and 13) and to a strong asymmetry in the plane of the interspersing species.

For the SiOxOy_1 models, the distortion induced by the insertion of oxygen into the silicon lattice leads to a reduction of the crystal symmetry from Fd3m to C1. This breaks the degeneracy of the symmetrically equivalent conduction bands minima of silicon along X, Y and Z. As a result, the electronic gap, defined between the k points with the coordinates

(0,0,0.0567) TVB and (0,0,0.0364) BCB becomes quasi-direct (and spans between 0.45 and 0.73 eV computed at the PBE level – Figure 13 – models Si4O0.5_1 to SiO8O0.5_1). Given that the PBE exchange correlation functional is known to underestimate seriously the values of the forbidden gap, we used the HSE hybrid exchange correlation functional and the Tran-Blaha one to improve its description. By default, the HSE functional is parameterized to account for a screening factor (α) of 0.25 that tends to over evaluate the band gaps of semiconductors. We followed the approach proposed by Alauskas et al{10} and tuned the screening factor going from 0.25 to 0.11 to obtain a correct evaluation of the silicon band gap. For Si4O0.5_1, this sets the computed band gaps at 1.14(HSE-α=0.11)/1.70 eV (HSE-α=0.25) and consistently, at 1.25 eV using the Tran-Blaha functional, i.e. at a value slightly larger than the bulk silicon one.

Compared to the bulk silicon case (Figure 10), the silicon atoms set in direct contact with the oxygen ones see the alignment of their orbitals in the conduction and valence bands reduced along the perturbation plane, which leads to the apparition of a narrow density of states at the bottom/top of the conduction/valence band at the k coordinates (0,0,0.0364) /(0,0,0.0567) (Figure 13). The situation is hence very different than for the bulk silicon one, where the bottom of the conduction [top of the valence] band is located to be close to the symmetry point X [Γ] and has a characteristic ellipsoidal [anisotropic] shape, as illustrated in Figure 12. Both the position and the shape of the bands are strongly impacted by the presence of the oxygen. In the valence band, a quasi-flat band appears in the Γ– Z direction and becomes the top of the valence band, while in the directions corresponding to the silicon plane, the bands get slightly steeper. This ‘new’ top of the valence band is quasi degenerated with the Γ point and lies at 0.11 eV of it for Si4O5_1.

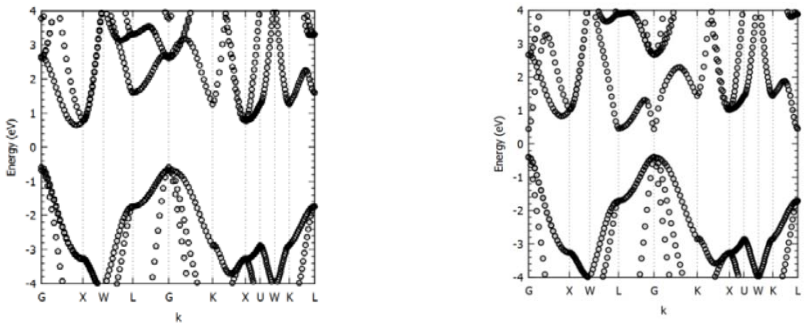

Figure 10: Illustration of the band structure of bulk silicon (left) and bulk germanium (right) computed using the Tran-Blaha exchange correlation functional.

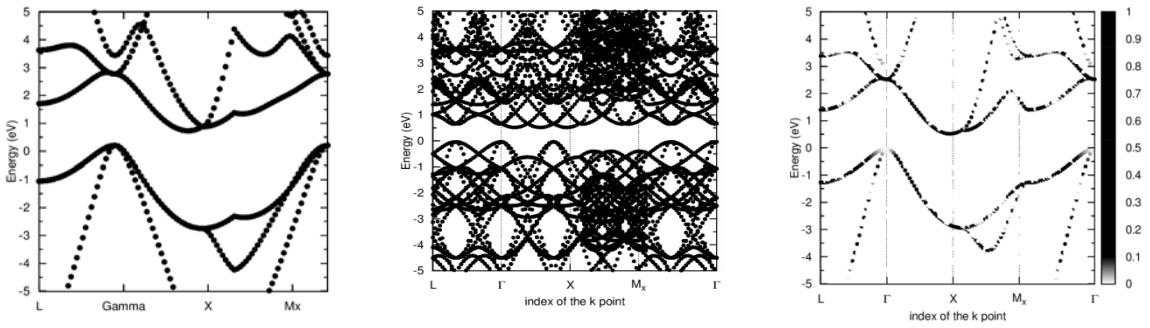

Figure 11: Evolution of the electronic structures of bulk silicon computed for a primitive (1x1x1) (left), a non-primitive (3x3x3) one (middle) and a Si (3x3x3) unfolded one using the approach proposed by Haverkort et al {19} (right).

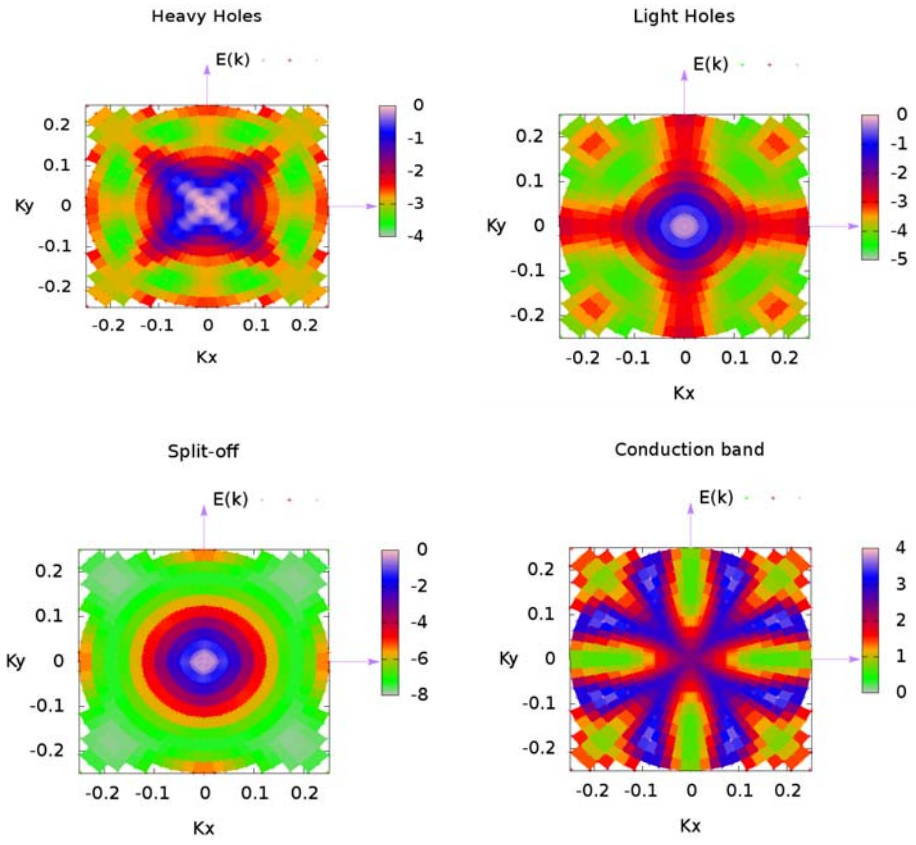

Figure 12: 2D energy versus k mapping of the bands structure computed at the top of the valence and at the bottom of the conduction bands for bulk silicon.

Also, the characteristic canonical shape present at Γ for the valence band of bulk silicon for the light and split-off bands is deformed, which leads to a band crossing. These changes are translated by an alteration of the effective masses (Figure 14), especially along the planes that contain the oxygen atoms, with fluctuations ranging from ~0.2 up to 3.5 me out of the plane. This implies a reduction of the mobility of the holes perpendicular to the plane. Unfortunately, the presence of the oxygen atoms also impacts on the effective mass in the silicon plane (labeled as XY in Figure 14). Interestingly, the bottom of the conduction band

maintains properties relatively similar to the bulk silicon with an average effective mass of 0.2 me that varies from 0.2 to 1 me out of the plane (Figure 14).

Increasing the number of silicon layers from 4 to 6 shifts the minima of the conduction bands along the X and Y directions towards higher energies. The Si layers gradually acquire their bulk behavior, which translates the role of the interspersing species as a 'confinement' source for the wavefunction (Figure 13). Along Z, a new band appears and defines the bottom of the conduction band. It also reduces the difference in energy between the 'flat' valence band and the maximum one formally located in Γ from 0.11 to 0.05 eV (below the valence band). These shifts alter slightly the computed band gap [1.26 eV (6ML)(Tran-Blaha)- 1.15 eV (6ML) (HSE α=0.11)], which remains defined between the k coordinates (0,0,0.65) and (0,0,0.121). However, the 'flatness' of the top of the valence band is translated by a significant increase of the hole effective mass along the Z directions but also along the X and Y ones (Figure 15). Similarly, the conduction band located in (0,0,0.65) is associated with a very large effective mass along the Z direction. This leads to an increase of the computed hole and electron effective masses by about two orders of magnitudes with respect to the bulk silicon case. Clearly, the combination of these two aspects is detrimental for both the electron and hole mobilities.

(Si4O0.5_1)

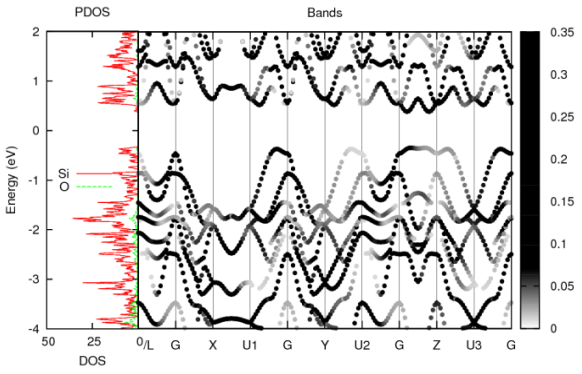

(Si6O0.5_1)

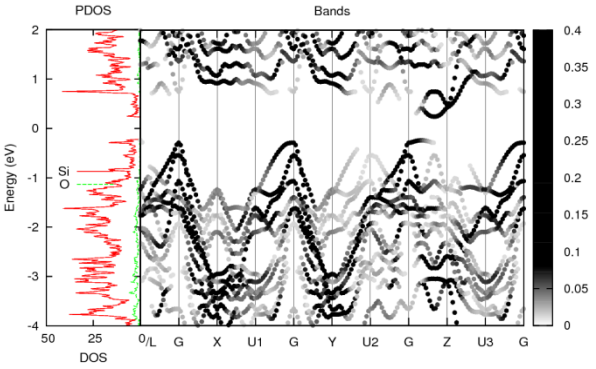

(Si8O0.5_1)

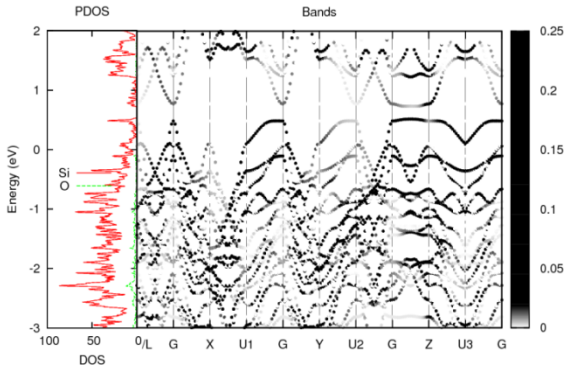

(Si3O0.5_2)

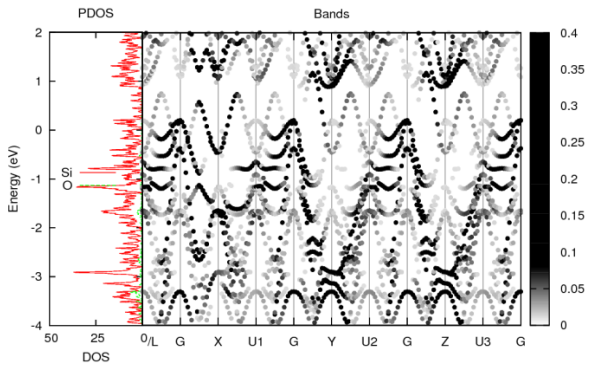

(Si3O1_2)

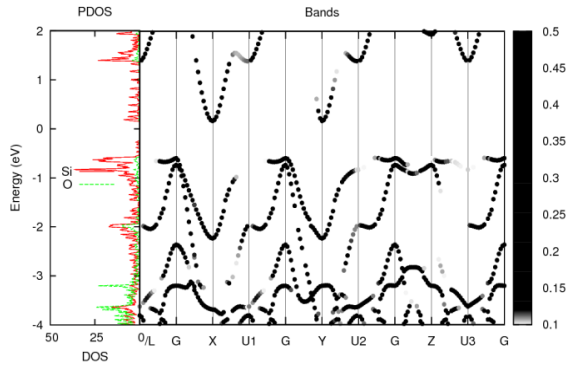

(Si7O1_2)

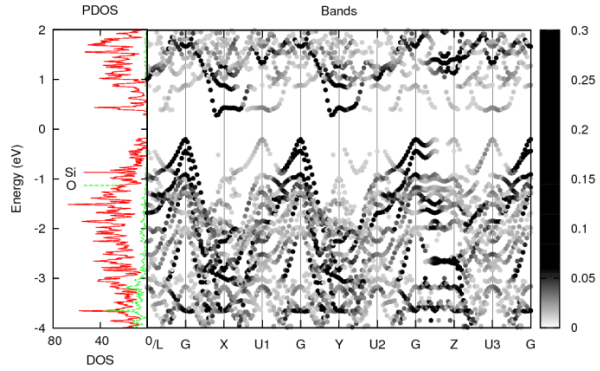

Figure 13: Evolution of the band structure computed at the PBE level along the main silicon symmetry k points for the SixOy_1 and SixOy_2 models with 4, 6 and 8 ML (model SixOy_1) and 3 and 7ML of silicon (model SixOy_2) combined with 0.5 and 1 ML of oxygen. The contribution of the oxygen to the partial density of states is colored in green. The total one is in red. The grey scale used to color the band structure reflects the weight of the $I^{\tau_i \tau'_i}_{b,k}$ coefficient computed in Eq.1 .

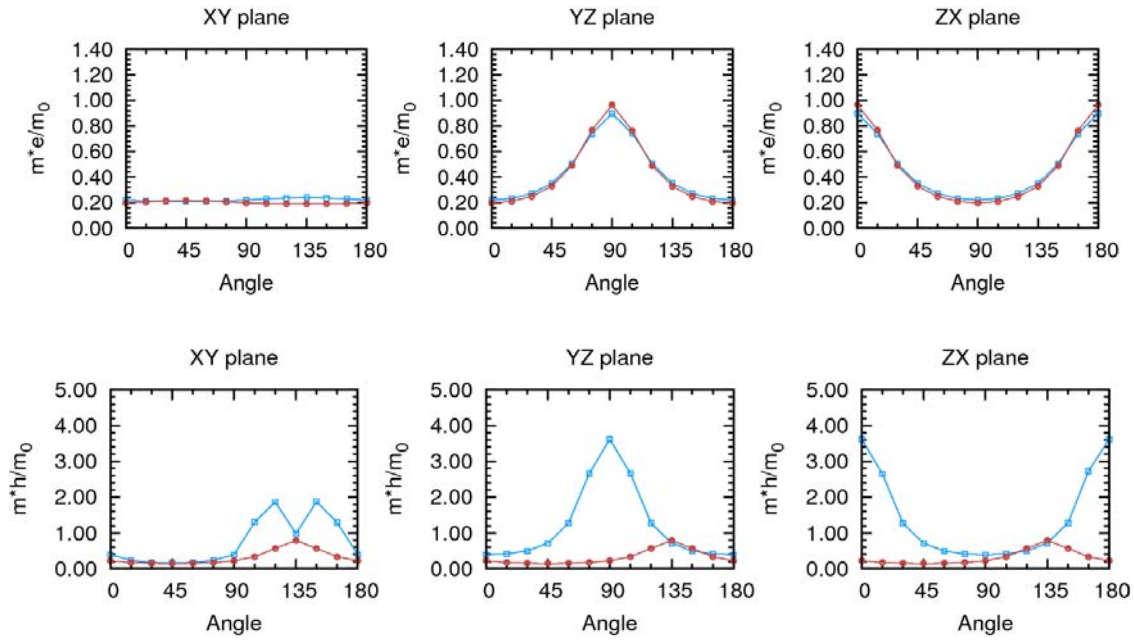

Figure 14: Electron (me) and hole (mh) effective masses computed in the XY, YZ and XZ planes (see Figure 7 for the axes convention), starting from the X to Y, Y to Z and X to Z directions in the k space (Brillouin zone) corresponding to the top of the valence (top) and to the bottom of the conduction bands (bottom) for the Si4O0.5_1 model (blue) and bulk silicon (red). The oxygen layer is placed along the Z direction.

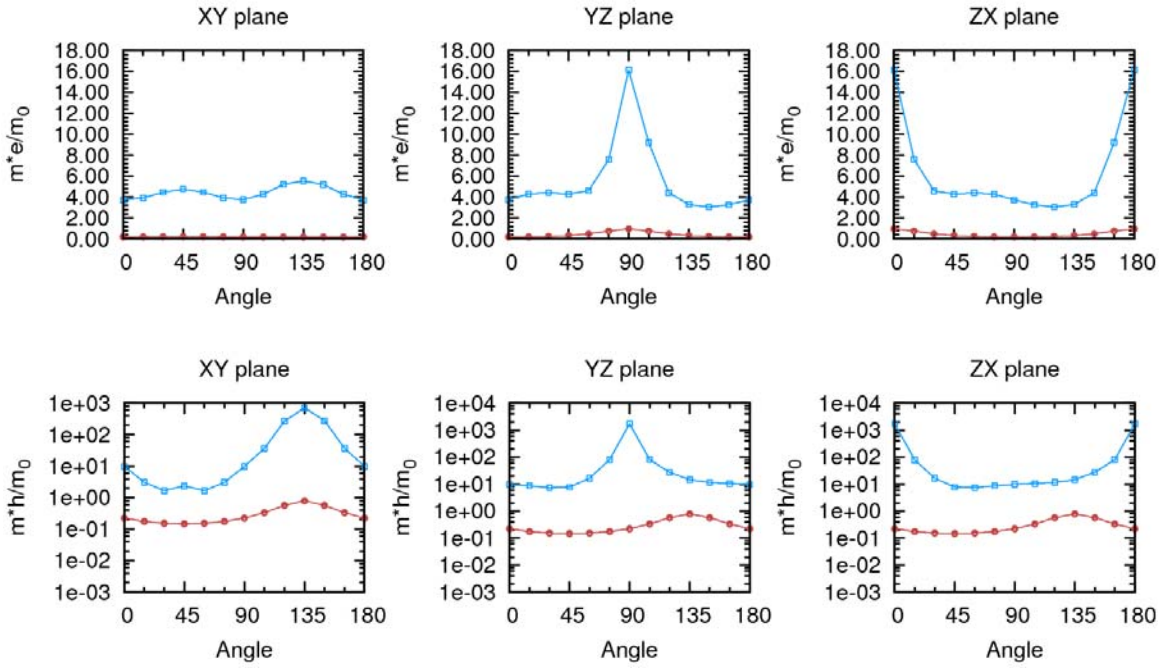

Figure 15: Evolution of the electron (me) and hole (mh) effective masses computed in the XY, YZ and XZ planes (see Figure 7 for the axes convention), starting from the X to Y, Y to Z and X to Z directions in the k space (Brillouin zone) corresponding to the top of the valence (top) and to the bottom of the conduction bands (bottom) for the Si6O0.5_1 model (blue) and bulk silicon (red). The oxygen layer is placed along the Z direction.

Switching the oxidation state of silicon from +1 to +2 lessens the band gap of the superlattice due to the reduction of the crystal symmetry, as suggested by the large amount of compressive strain (15%) present in Si3O0.5_2 (Figure 18). On the other hand, increasing the concentration of the inserted oxygen in +2 oxidation state to 1ML (model SixOy_2) restores the crystal symmetry and enlarges the band gap to 2.25 eV (Tran-Blaha) (Figure 18). In this configuration, the stack has an indirect band gap with 2 degenerated conduction bands located close to the X/Y symmetry points (Figure 13– SiO3_1_2). However, along the direction of the perturbation, the bottom of the conduction is shifted upwards by ~ 1.5 eV. The top of the valence band shows a pattern qualitatively similar to the one of bulk silicon at Γ, at the difference that in the directions of the oxygen plane, the band gets flatter. The symmetry and the strain imposed by the +2 oxidation state in the silicon plane leads to an increase of the electron mass along all the directions compared to bulk silicon. The situation is similar for the holes (Figure 16).

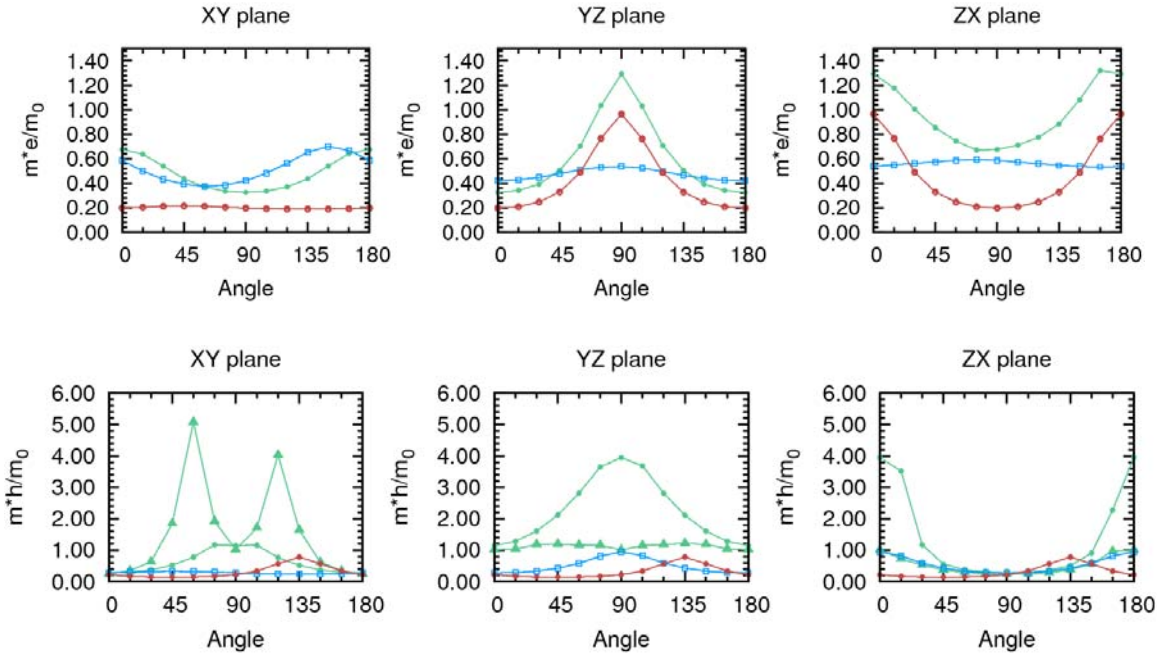

Figure 16: Electron (me) and hole (mh) effective masses computed in the XY, YZ and XZ planes (see Figure 7 for the axes convention), starting from the X to Y, Y to Z and X to Z directions in the k space (Brillouin zone) corresponding to the top of the valence (top) and the bottom of the conduction bands (bottom) for the Si3O1_2 model (green)/Si7O1_2(blue) and bulk silicon (red). The oxygen layer is placed along the Z direction. Note that for the Si3O1_2 model, there are two close lying top of the valence bands located along the Γ-Z (closed triangle) and in the Γ points (closed circle).

Increasing the number of Si layers to 7 leads to a conservation of the band gap value [0.49 eV PBE/1.18 eV (HSE-α=0.11)/1.45 eV (Tran-Blaha)]. However, the shape of the minimum and of the maximum of the valence and conduction bands is changed by the deformation induced by the Si-O bonds. The latter takes over the quantization effects generated by the confinement of the oxygen atoms on the wavefunction. The strain built in the silicon layers leads to a stabilization of the 'bulk silicon' conduction minimum valleys and to a reduction of

the electron effective masses with respect to Si3O1_2. Compared to bulk Si, the averaged me and mh values are almost equivalent.

A rotation of the substrate, i.e. going from (100) to (111) leads to a reduction of the band gap [0.26 eV PBE – 0.95 eV (HSE-α=0.11) - 0.98 eV (Tran-Blaha)]. Along this plane, Si adopts a Si+1 oxidation state in contact with the oxygen atoms, similarly to the Si4O0.5_1 (100) model (Figure 17). The electronic properties and the crystal symmetry being driven by the directionality of the strain induced by the oxygen bonds, these changes are reflected into the effective masses. As a result, the top of the valence band is located between the L and Γ bulk silicon symmetry k points and the bottom of the conduction band in X. The change in the orientation of the oxygen plane is reflected in the anisotropy of the electron and hole effective masses. At the difference of the (100) plane, the electron effective masses are no longer isotropic in the silicon plane and vary between 0.2 to 0.75 me. This is translated by an increase of the electron effective mass to values close to the bulk silicon ones. The strain induced by the formation of Si-O bonds impacts on the hole effective mass by shifting the maximum of its distribution in the XY plane by ~90°, while maintaining roughly the amplitude of the distribution quasi unchanged. Interestingly, the effective mass anisotropy is significantly reduced to be almost constant along the YZ and ZX planes.

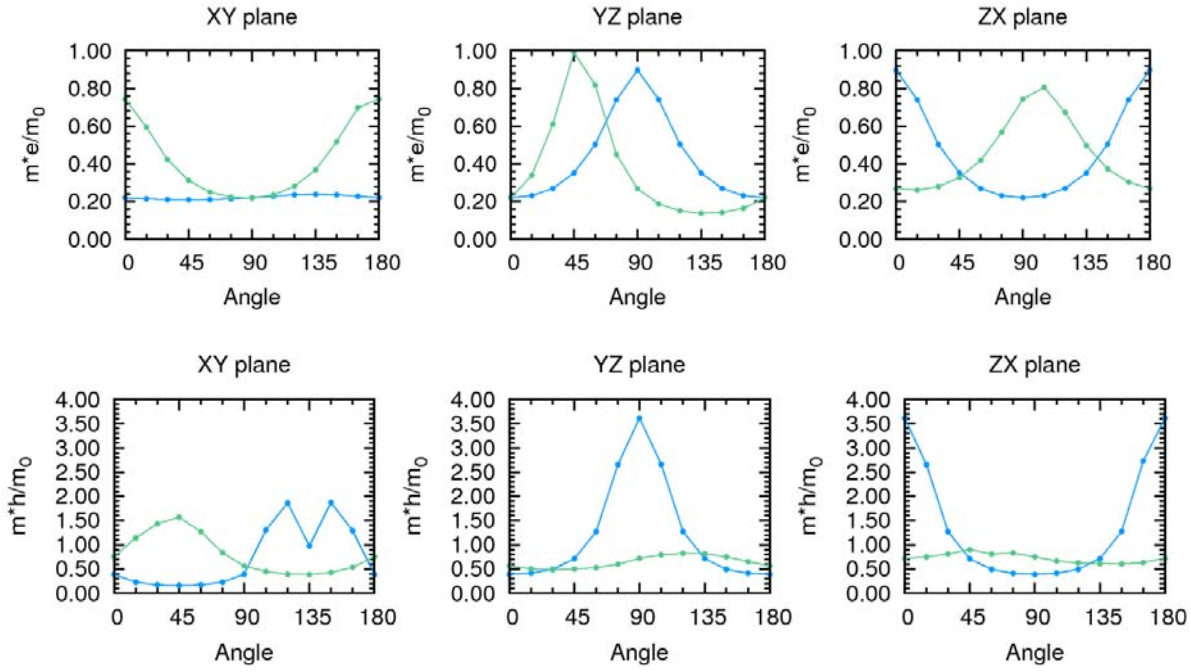

Figure 17: Evolution of the electron (me) (top) and hole (mh) (bottom) effective masses computed for a Si4O1 (111) superlattice in the silicon plane (XY) and out of it (YZ, XZ) (green) compared to Si4O_0.5(100) (blue). The oxygen are placed along the (111) direction in the Si4O1(111) model.

Switching from silicon to germanium leads to trends similar to the ones reported for the silicon superlattices. Oxygen induces a compressive strain whose amplitude is such that only the models with the oxidation state Ge+1 (GexOy_1) would lead to an unrelaxed epitaxial network (Figure 18). Its impact on the band structure is however more marked than for the silicon case: Indeed, for Si, the insertion of 1ML of oxygen slightly increases the gap, going

from 1.2 to 1.45 eV (Figure 18 -Si4O1_1), while for Ge, it leads to its reduction to about half of its bulk value.

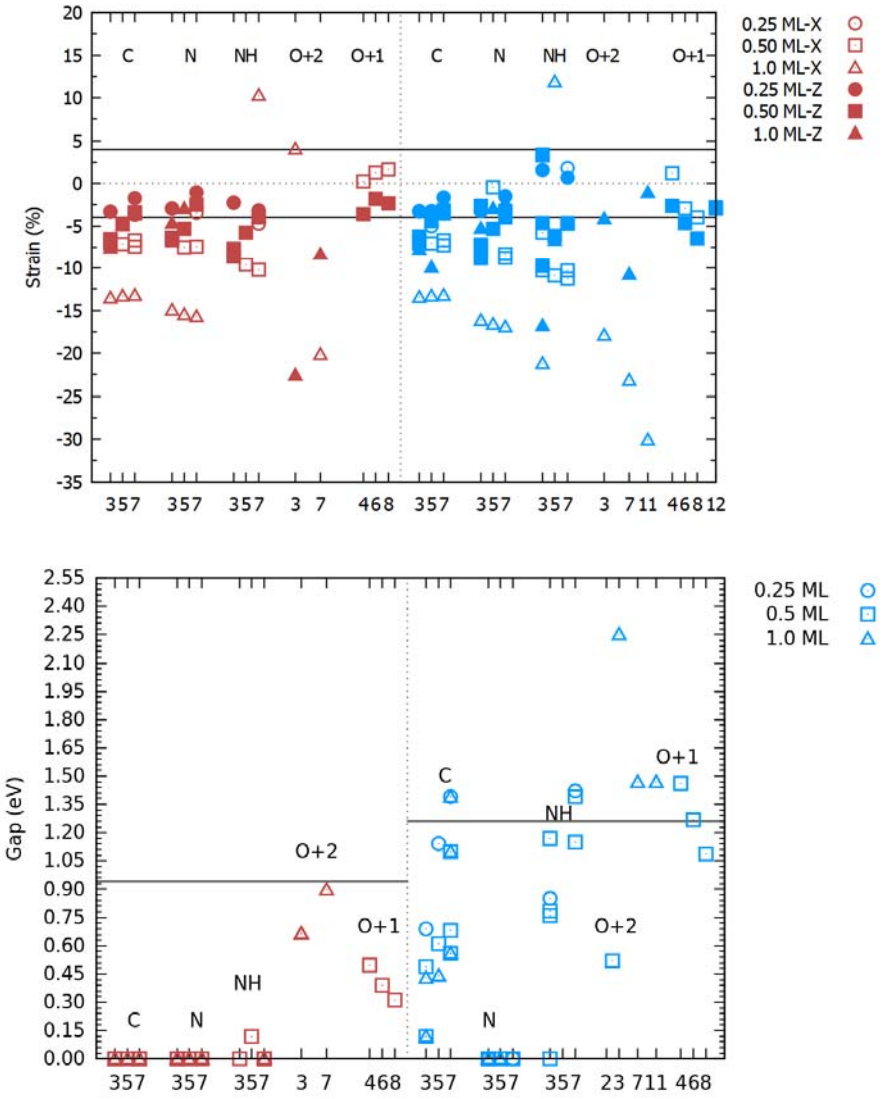

Figure 18: (top) Evolution of the strain computed with respect to the lattice constant of bulk silicon (blue) (5.41 Å - PBE level) and bulk germanium (red) (5.79 Å - PBE level). The number of layers used in the superlattice is labelled in abscisse. The triangle, squarre and circle correspond to 0.25, 0.5 and 1.0 monolayer introduced into the Si/Ge lattice. Filled and emptied symbols underline the strain felt along the X (label X in the inset) and Z (label Z in the inset) axes of the superlattice. The horizontal lines correspond to the maximum tensile and compressive strain deformations (±4%) that can typically be supported by bulk silicon/germanium before undegoing a lattice relaxation. O+1 and O+2 correspond to the two models used to build a superlattice with Si/Ge in the +1 (SixOy_1) and +2 (SixOy_2) oxidation states. NH labels the models computed for an hydrogen atom inserted intertitialy between a silicon/germanium atom in the neighborhood of a nitrogen center. All the computation have been carried out using the PBE exchange correlation functional. (bottom) : Evolution of the electronic gap with respect to the number of silicon (blue) and germanium (red) layers. The horizontal lines correspond to the germanium (left) and silicon (right) band gaps. All the computations have been carried out using the Tran-Blaha exchange correlation functional {11}. The color code convention used is similar to the top one of the figure.

Growing the number of semiconducting layers from 4 to 8 ML leads however to the same monotonous reduction of the gap. We attribute this difference to the combination of the alignment of the oxygen band/orbitals with the bottom of the conduction band of germanium, which is slightly different than for the silicon case and to the impact of the stress on the conduction band of germanium. Indeed, the minimum of the conduction band of germanium is located in the symmetry point L (degenerated six times), .i.e. along the direction of the densest atomic plane of germanium (111). In silicon, the gap is defined based on six equivalent valleys located along the [100] symetricaly equivalent directions. As a result, the contraction of the bonds induced by the insertion of the oxygen atoms leads to larger strain components along the (111) plane and hence squeezes asymmetrically the Brillouin zone. The top of the valence band is shifted from Γ (bulk) to a symmetry point located between Γ and Z. The bottom of the conduction band is shifted from L (111) (bulk) to Γ. Interestingly, the shape of this 'new' bottom of the conduction band is more symmetric and has a highly reduced effective mass compared to bulk germanium (Figure 20). The latter is lessened, going from a distribution spanning from 0.15 to 0.28 me to 0.05-0.07 me. This has also a direct impact on the distribution of the hole effective masses, leading to a more symmetric valence band, with an improved hole mobility in all the planes. For instance, in the YZ one, the hole effective mass is reduced up to a factor 6 with respect to its bulk value. Going from 4 to 6ML of Ge helps recovering partially the anisotropy of the bands, which is reflected by an increase of the electron and hole effective masses (whose averaged values lie close to the germanium bulk one).

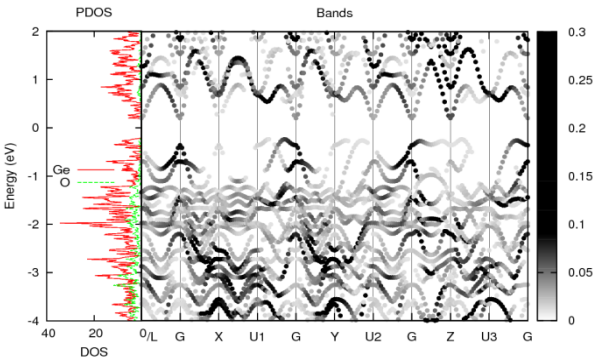

Figure 19: Band structures and partial density of states computed for the Ge4O1_1 model using PBE+U. The zero is set to the Fermi level.

Changing the oxidation stage from +1 to +2, i.e. going from model GexOy_1 to GexOy_2, shows similar trends to the ones reported above: the electron effective mass is significantly reduced in the XY plane, independently of the germanium thickness used, while out of the plane, it is slightly reduced/increased in the direction of the added oxygen atoms (Figure 21). Similarly, at low germanium thickness (3ML), the hole effective mass is largely reduced in the XY plane, while in the perpendicular ones, they remain relatively large. The augmentation of the number of germanium layers leads to a significant enlargement of the hole effective mass, both in plane and out of the plane.

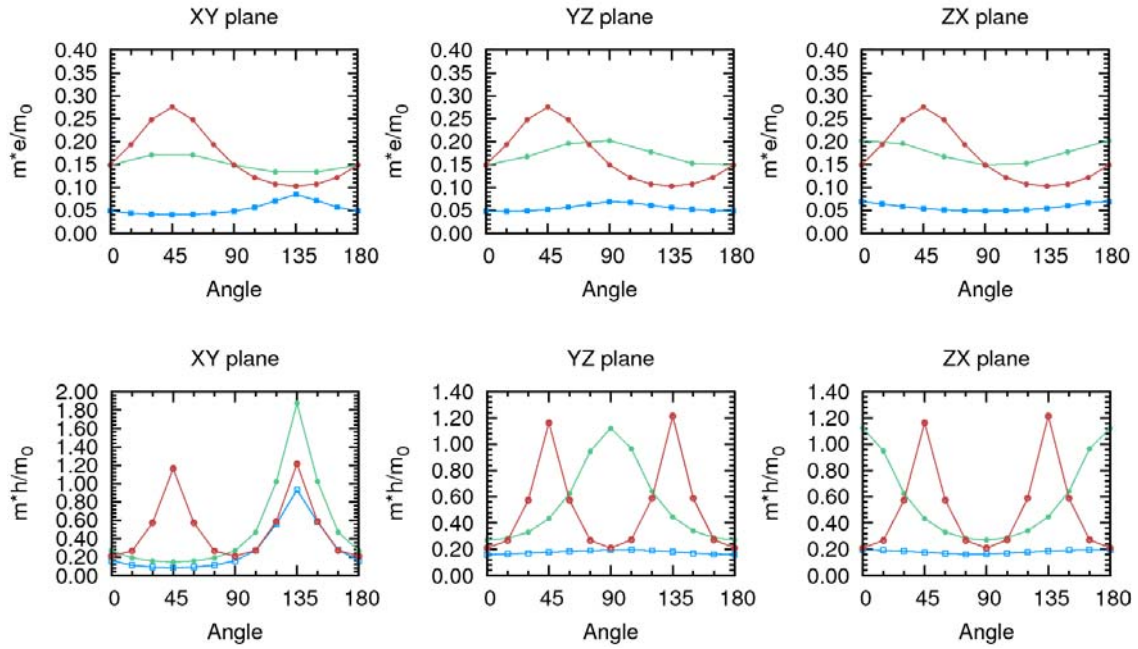

Figure 20: Electron (me) and hole (mh) effective masses computed in the XY, YZ and XZ planes (see Figure 7 for the axes convention), starting from the X to Y, Y to Z and X to Z directions in the k space (Brillouin zone) computed for the top of the valence (top) and the bottom of the conduction bands (bottom) for the Ge4O0.5_1 model (blue), Ge6O0.5_1 (green) and bulk germanium (red). The oxygen layer is placed along the Z direction.

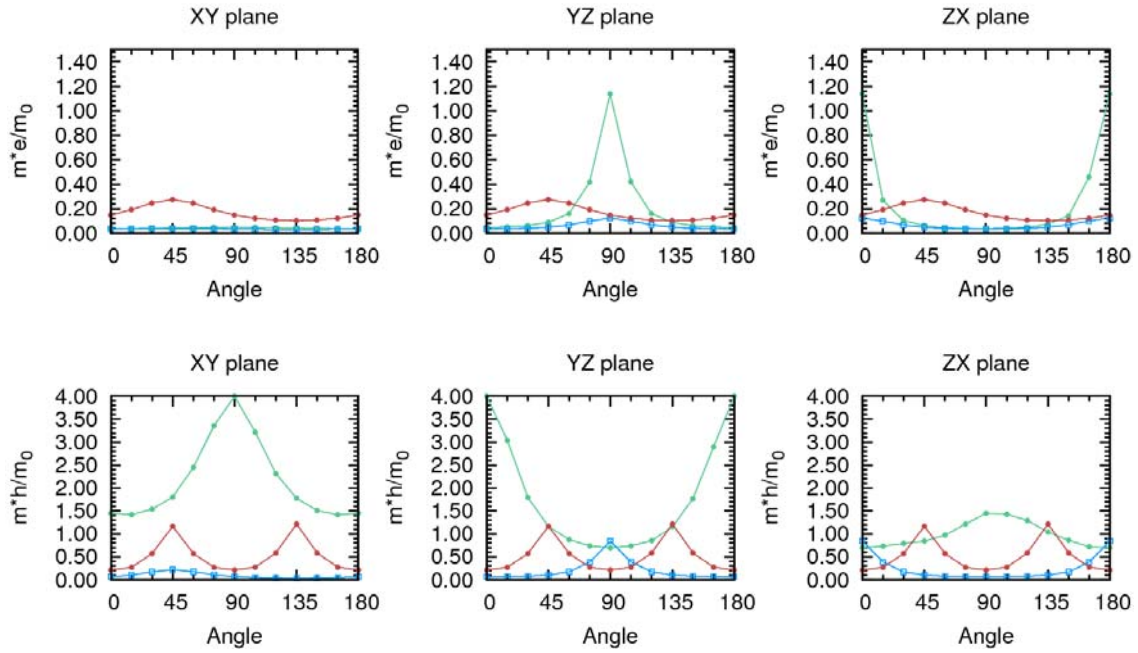

Figure 21: Electron (me) and hole (mh) effective masses computed in the XY, YZ and XZ planes (see Figure 7 for the axes convention), starting from the X to Y, Y to Z and X to Z directions in the k space (Brillouin zone) for the top of the valence (top) and the bottom of the conduction bands (bottom) for the Ge3O1_2 (green)/ Ge7O1_2 (blue) models and bulk germanium (red). The oxygen layer is placed along the Z direction.

Interestingly, while the expected performance improvements in terms of hole mobility is rather modest for thin Ge/GeO slabs (by about a factor two, based on the effective mass), the impact on the electron mobility in the germanium plane is more important and sets the effective mass of the superlattice, close to the ones reported for some III/V semiconductors, reported to be among the highest mobility materials. Similarly to the silicon case, the generation of a +2 oxidation stage leads to the accumulation of a large strain into the stack that is expected to induce a lattice relaxation process during the growth of the material. This suggests that a structure built on the +1 oxidation stage is likely more realistic than a +2 one. Still, a thin germanium superlattice could help smoothening the electron effective mass of germanium to more isotropic values and hence enhancing its mobility.

1.3.2 Nitrogen based superlattices

We used the methodology developed for the Si/SiOx case to study the nitridation process of silicon {2x1} (100). For the sake of simplicity, a convention similar to the one defined to monitor the oxidation degree of silicon has been chosen for the notation: whenever a silicon is bound to 1 nitrogen, it is referred as being +1, to 2, +2,...

At room temperature (Figure 22) and at low fluence, the nitridation process is dominated by the chemisorption of nitrogen on the dimers of the silicon surface. The presence of Si+1 remains stable up to a fluence of 1 monolayer (ML), as from which, traces of Si+2, Si+3 and Si+4 gradually appear. Similarly to the oxygen case, the kinetic of formation of a high nitridation coordination number for silicon is slower than for the low ones.

Increasing the temperature or the fluence promotes the diffusion and the reactivity of the nitrogen atoms with the substrate. As a result, going from 498 to 698 K leads to a reduction of the fluence threshold as from which, the conversion of the Si+1 species into Si+2, Si+3 and Si+4 occurs.

At 298K and at low fluence, the nitrogen diffusion and its reaction with silicon are mainly cantoned within the first 5 Å of the silicon slab, limiting the reaction to the silicon surface dimers only (Figure 22).The surface, i.e. the Si-Si dimers, is hence fully saturated with nitrogen atoms and the reaction does not evolve anymore within the simulated time window. Raising the temperature to 498K or the fluence, enhances the diffusion of nitrogen into the substrate up to ~ 1nm below the surface (which is translated by a raise of the Si+1 population in the slab between 0.5 to 1nm). The increase in thermal energy also favors the nitridation process and promotes the formation of Si+2 and Si+3 close to the surface (0 to -0.5 nm) and the expansion of SiNx (0.5nm to 0nm) (not shown). Similarly to the oxygen case, we find that the on-top (T), back-bond (B), and dimer-bridge(D) configurations are present on the {2x1} Si(100) surface (Figure 5). The T configuration is found as soon as the first subsurface layer becomes nitrided. The Si+2 peak indicates the apparition of two bonds, that are typically of the BB, DB or BT or types, of which the BB and BD ones dominate. As the nitridation proceeds, the Si+1 peak is gradually reduced while the Si+2 and Si+3 ones grow to coexist. As from a fluence of 1.5ML, the signature of Si+4 gradually appears on top of the

nitrided surface. Naturally, nitrogen tends to saturates its 3 valence electrons to minimize the number of dangling bonds. This is shown by the apparition of Si+2 and Si+3 at low fluences during the nitridation process. Switching from a (100) to a (111) orientation promotes the generation of Si+2 and Si+3 with respect to the (100) case (Figures 22 and 24).

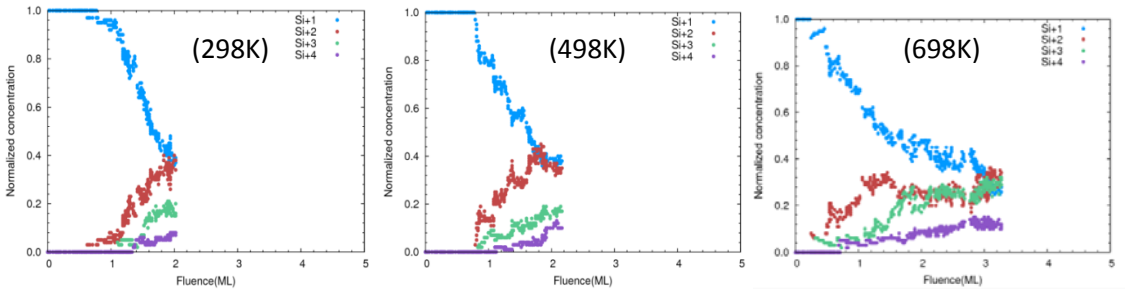

Figure 22: Evolution of the nitridation process of silicon with respect to the fluence computed on {2x1} Si(100) using atomic nitrogen at 298, 498, 698 K.

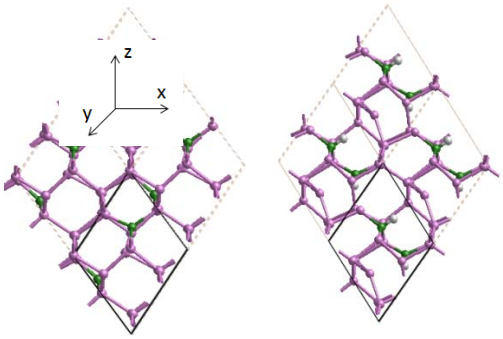

Figure 23: Illustration of the Si/SiN superlattice models used. Silicon, nitrogen and hydrogen are colored in pink, green and white, respectively

Given the similarity of the results and for the sake of concision, we combined the discussion of the computed properties of silicon with the germanium ones in the coming paragraphs. Starting from the hypothesis that Si+1[Ge+1] (T) is the dominating oxidation state at the Si(100) [Ge(100)] surface and using the topologies reported in Figure 23, we built a set of representative models of epitaxial Si/SiNx [Ge/GeNx] superlattices (Figure 25). Nitrogen brings an additional degree of complexity with respect to the oxygen case due to its number of valence electrons. Indeed, while oxygen organizes its 6 valence electrons into two pairs and two unpaired ones, which brings some structural flexibility into the formation of two bonds with the silicon atoms during the epitaxy, nitrogen has, on the contrary, three unpaired electrons and two paired ones. This leads to the formation of 3 Si-N [Ge-N] bonds to fulfill the valence shell. Each Si-N [Ge-N] bond is significantly shorter than the Si-Si [Ge-Ge] one and spans from 1.70 to 1.85 Å [2.02 to 2.16 Å], which accumulates compressive stress around the nitrogen center. Also, the steric hindrance associated to the presence of three Si-N [Ge-N] bonds and to the nitrogen free electron pair leads to the formation of Si-N-Si [Ge-N-Ge] angles that range from 106 to 120 degrees and deviate significantly from the tetrahedral structure characteristic of bulk Si (109.7 degree). The introduction of nitrogen and the combination of changes in bond lengths and in angular distribution induces a large source of

stress in the lattice (Figure 18). This suggests that the growth of epitaxial Si-SiN [Ge-GeN] superlattices will be difficult to achieve, as suggested by Waltenburg et al {20}, and that the system will minimize the stress accumulated through the relaxation of the epitaxy.

Chemisorbed in a T1 configuration (Figure 5), nitrogen can either maintain its local coordination to 3 during the growth, leading to the formation of an unsaturated Si [Ge] dangling bond per nitrogen site (Si [Ge] had to be bounded 4 times to maintain its tetragonal symmetry) which could then be passivated by an hydrogen atom during the growth process or promotes the amorphization of the grown layers. Alternatively, the free electron pair of nitrogen can also be shared with a silicon atom in its neighborhood to adopt a tetragonal–like configuration, as found in high pressure γ-Si3N4 {21}. In the latter case, each nitrogen atom has an unsaturated electron that dopes the Si matrix. Figure 18 shows that the substitution of silicon by nitrogen within an ideal superlattice leads to the accumulation of a large amount of compressive strain. The latter increases with the concentration of nitrogen and spans from ~3.2 % for 0.25ML to ~ 16% for 1ML of nitrogen (3ML Si [Ge]). Given that silicon [germanium] can typically accommodate up to 4% before undergoing a strain relaxation process, this suggests that a 4 times coordinated N center could potentially be present up to ~0.4 ML in the superlattice (Figure 18). Note that the value is not absolute since, at low concentrations, the distribution of the nitrogen atoms can adopt different patterns, being either an in-line or a chess-like configuration. This leads to a spread in the computed strain values as shown in Figure 18.

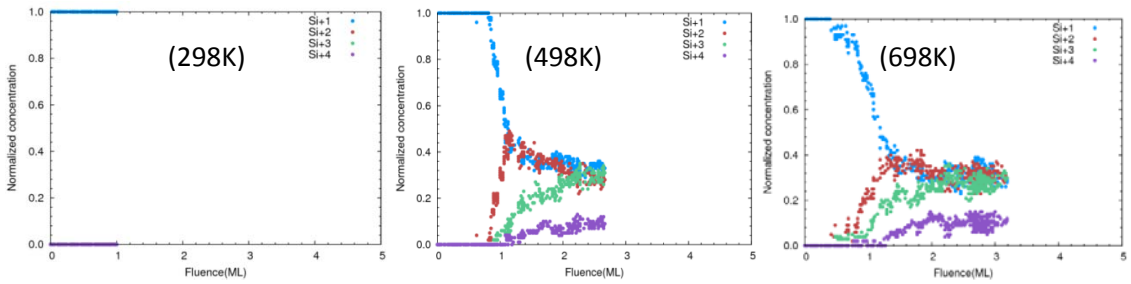

Figure 24: Evolution of the nitridation process of silicon with respect to the fluence computed on Si(111) using atomic nitrogen at 298, 498 and 698 K.

Increasing the number of Si [Ge] monolayers in SixNy [GexNy] reduces the strain along the Z direction but does not significantly alter it along the other ones. Due to the stress accumulation and of the contribution to the additional electron in the network, the Si/SiN [Ge/GeN] superlattices are metallic, implying that N acts as an electron donor as shown by the crossing of the bands (Figures 18 and 26), which prevents the fitting of meaningful effective masses (Figure 26).

The introduction of an hydrogen atom into the lattice between the nitrogen site and one of the silicon [germanium] atom anchored to it, prevents the free electron pair of nitrogen to be shared with a silicon [germanium] site and induces a strong atomic relaxation into the lattice (Figure 25): the strong steric hindrance induced by the insertion of an additional hydrogen and the dense packing of silicon [germanium] pushes the nitrogen atom together with the three silicon [germanium] ones present in its coordination shell out of its symmetric

tetragonal position to adopt a trigonal one, typical to the Si3 centers found in α and β Si_3N_4. This atomic relaxation leads to a wider spread in the distribution of the lattice strains (by 5%) compared to the non-hydrogenated system but does not alter the threshold of the number of nitrogen monolayers that the system can accommodate before relaxing.

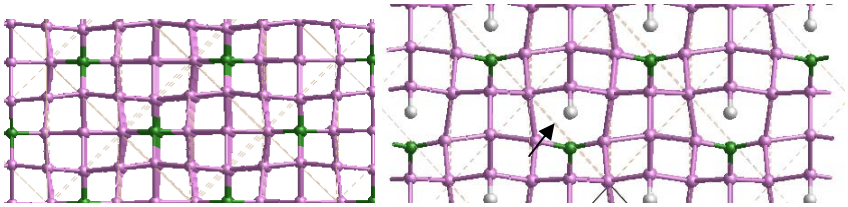

Figure 25: Illustrations of a Si3N0.5 superlattices without (left) and with an interstitial hydrogen (right) placed in the coordination shell of the nitrogen center. The geometry relaxation associated with the insertion of hydrogen is indicated with an arrow. Silicon, nitrogen and hydrogen are colored in pink, green and white, respectively.

The geometric pattern chosen in the crystal for the insertion of the nitrogen and of the hydrogen sites leads to either a reduction or to an increase of the strain accumulated into the lattice (Figure 18). It however stabilizes the system by ~3.6-3.7 eV [~4.2 eV] per hydrogen atom, independently of the number of Si [Ge] layers. The impact on the absolute value of the electron and hole effective masses is driven by the directionality of the Si-N bonds. The distribution remains however qualitatively unchanged, going from one pattern to another one. As an illustration, we report in Figure 28, the distribution of the hole and electron effective masses computed for 3, 5 and 7 ML of Si in presence of 0.5 and 0.25 ML of nitrogen and hydrogen (Si3N0.5_H, Si5N0.5_H and Si7N0.25_H). For thin Si layers, the N(H) sub-monolayer reduces the anisotropy of the bottom of the conduction band with respect to bulk, implying that the band structure does not feel the nitrogen layer as an hindrance for the electron mobility. For the holes, it enhances it out of the Si plane. A Si thickness of 7 ML leads to the reverse effects, with a strengthening of the anisotropy out of the Si plane for the electron and a weakening one for the hole. Given the presence of hydrogen during the typical Chemical Vapor Deposition (CVD) process, this topology is hence likely to occur. The insertion of hydrogen induces a non-metallic character for the Si superlattices and opens a band gap that spans from 0.7 to 1.2 eV (Tran-Blaha), as long as the concentration of nitrogen inserted remains lower than 0.5ML. For the Ge systems, the structures remain metallic.

We have also checked the impact of the formation of a silicon [germanium] vacancy in the neighborhood of nitrogen. It favors the relaxation of the stress accumulated in the layer and the reduction of the epitaxial character. However, the energetic cost of the generation of such a defect is relatively high (4.02 eV) and is found to be in the same order of magnitude as the bulk silicon one (3.7 eV). It also leads to the generation of a high density of defects and hence, a metallic character to the system.

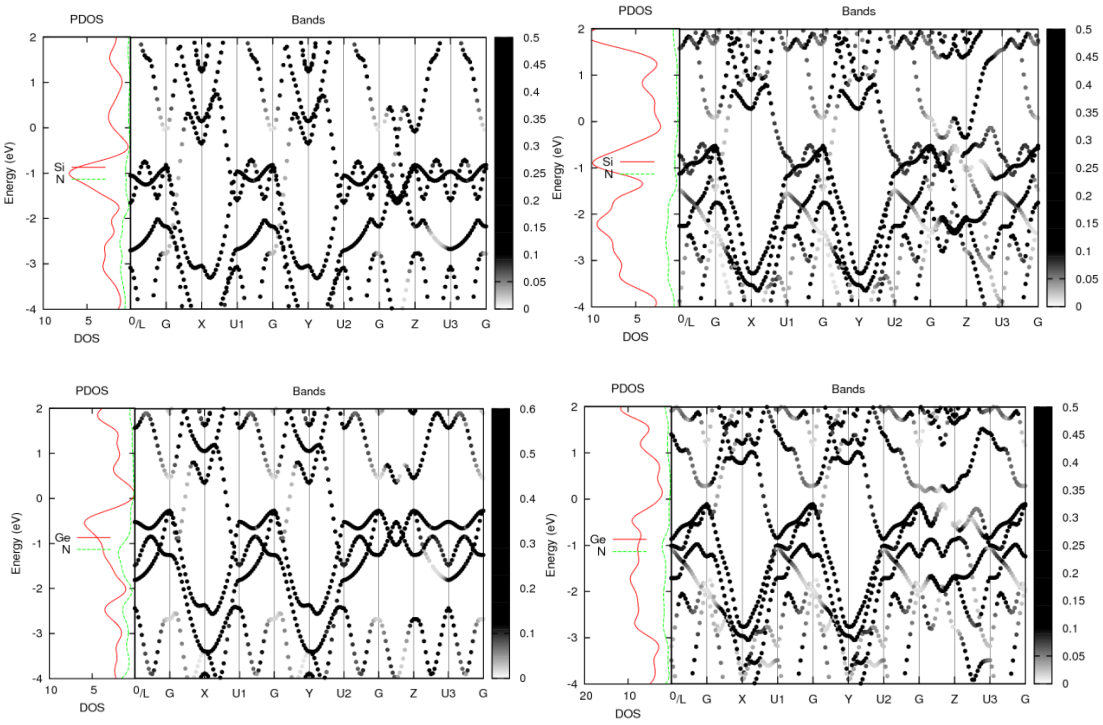

Figure 26: Band structures and partial density of states of Si3N1 (top left)/Ge3N1 (bottom left) and Si5N1 (top right)/Ge5N1(bottom right) superlattices computed at the PBE level. The zero is set to the Fermi level.

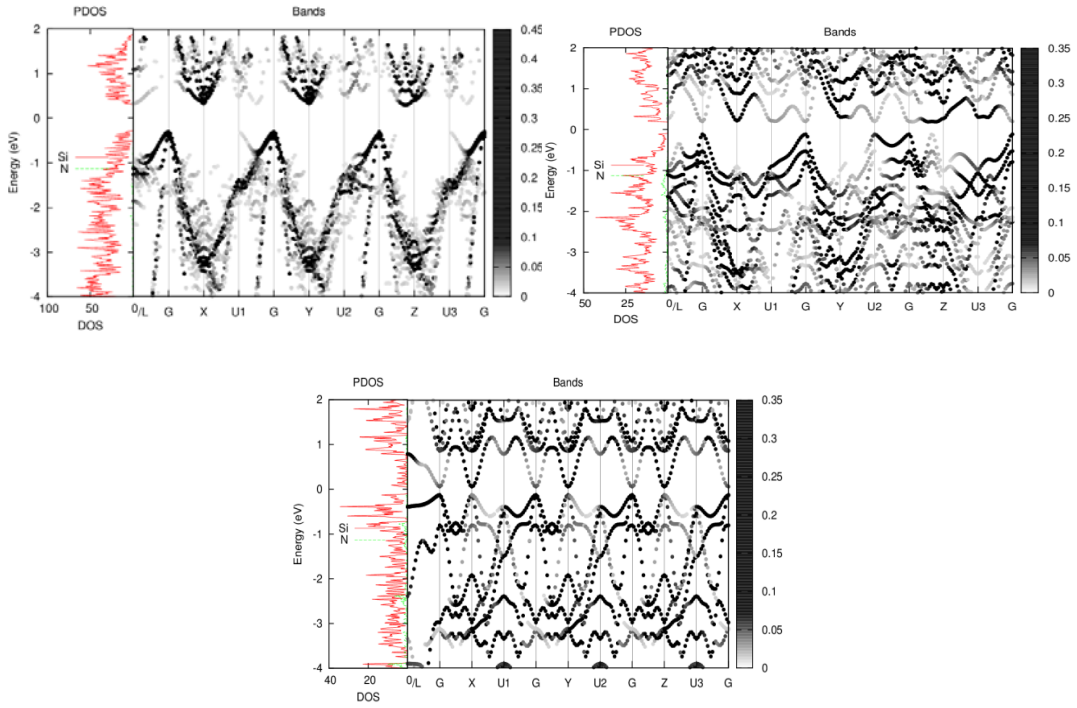

Figure 27: Band structures and partial density of states computed for the Si7N0.25_H (top left) and Si5N0.5_H (top right), Si3N0.5_H (bottom) superlattices computed at the PBE level. The zero is set to the Fermi level

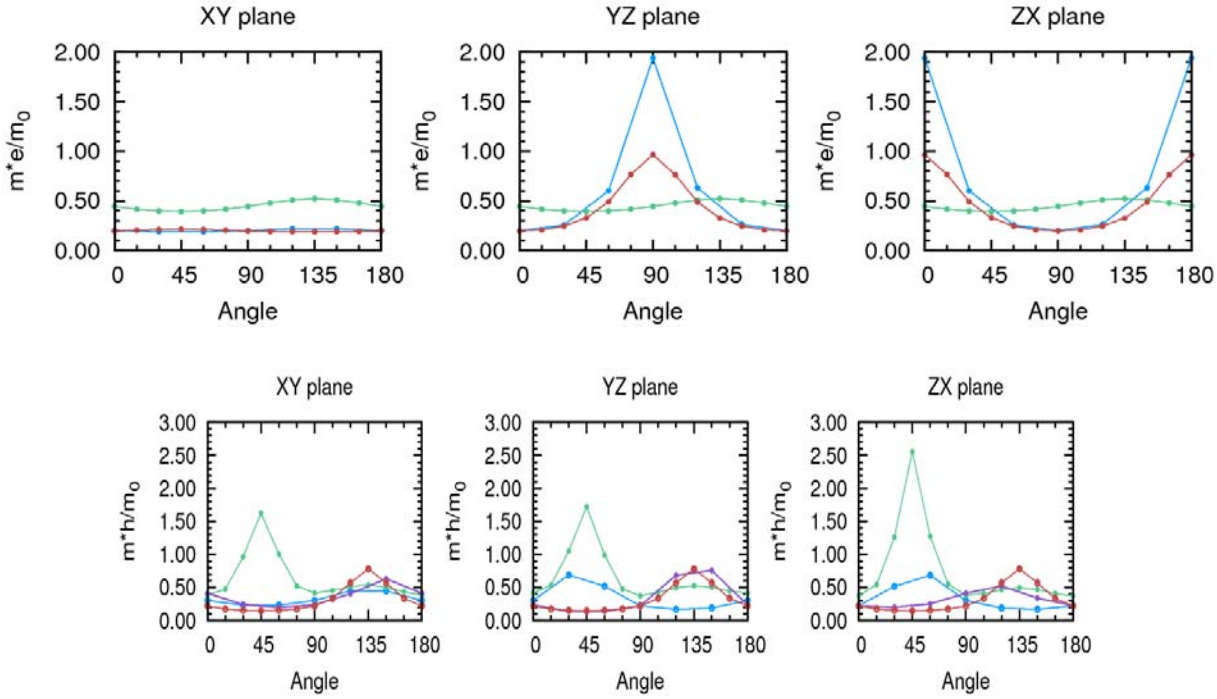

Figure 28: Electron (me) and hole (mh) effective masses computed in the XY, YZ and XZ planes, starting from the X to Y, Y to Z and X to Z directions in the k space (Brillouin zone) corresponding to the top of the valence (top) and the bottom of the conduction bands (bottom) for the non-metallic Si3N0.5_H (green) ,Si5N0.5_H (purple), Si7N0.25_H(blue) models and bulk silicon (red). The oxygen layer is placed along the Z direction.

1.3.3 Carbon based superlattices

The deposition of C using CVD on a silicon substrate to grow SiC films is a well-documented process (see for instance references {22-23}). Typically, bulk SiC can coexist in numerous different crystal structures. The most commonly used ones in electronics are the 3C-SiC (cubic), 6H-SiC, 4H-SiC (hexagonal) and 15R-SiC (rhombohedral) phases. The development of epitaxial Si/C superlattices implies the conservation of the crystal symmetry of Si. Hence, only the cubic phase of SiC (3C-SiC) is susceptible to match with the silicon FCC one. In this phase, the carbon atoms occupy the center of a tetrahedral configuration, which maintains the crystalline symmetry of bulk Si. Given that the growth mechanisms are well known, we focused only the electronic properties of the superlattices.

The difference in atomic sizes of the covalent radii of carbon and silicon is such that the Si-C [Ge-C] (1.88Å) [(2.18 Å)] bonds are 20% [15%] shorter than the Si-Si [Ge-Ge] one (2.35Å) [2.51 Å]. Similarly to the oxygen and nitrogen cases, this results to the accumulation of large a compressive strain into the Si/C [Ge/C] superlattices (Figure 18). However, at their difference, C has less flexibility to accommodate the directionality dependence imposed by the angular constraint (109.7 degree) of its four Si-C [Ge-C] bonds. As a result, the strain induced into the superlattice is larger than in the Si-O [Ge-O] case but also more isotropic. This sets an upper limit to the amount of carbon that can be introduced into the lattice to

0.5ML before the superlattice relax itself. 0.5 ML of C leads to a reduction of the band gap of the Si/SiC lattices to a range of values spanning from 0.15 to 0.6 eV, depending on the pattern chosen to position the C atoms. For instance, if the atoms are inserted in lines, the accumulated strain is larger than in a chess-like pattern. Figure 18 shows that the band gap is very much dependent on the number of Si layers present into the stack; the thinner the silicon layers, the smaller the band gap. The system recovers partially the electronic gap of bulk silicon as from 7ML of Si with values distributed from 0.55 to 1.40 eV. Note that the border of the interval found at 1.40 eV is likely an overestimation of the bulk Si band gap value due to some fluctuations of the screening term computed within the Tran-Blaha functional.

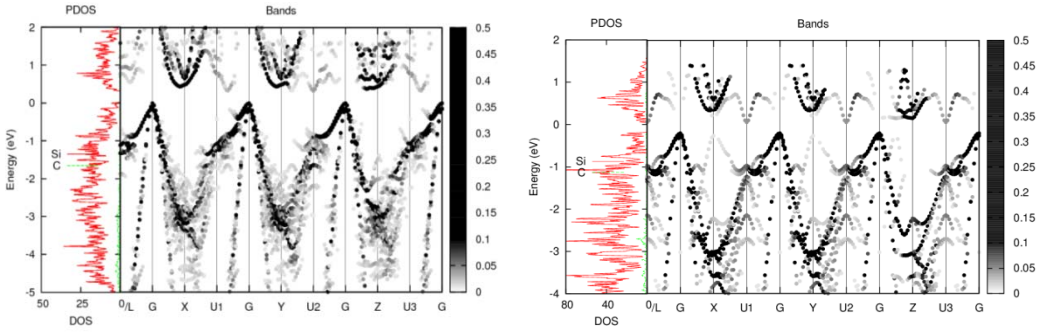

Figure 29: Band structures and partial density of states of Si5C0.25 (left) and Si7C0.5 (right) computed at the PBE level (the band gap is underestimated by ~ 50 %). The zero is set to the Fermi level.

The pattern of the computed band structure is relatively similar for all the C based models (see for instance Si5C0.25 and Si7C0.5 in Figure 29). As expected, the system symmetry 'protects' the band structure from the perturbation and preserves most of the bulk Si features. The difference between the planes where the C sub monolayers lie and the Si (XY) layers are hence less marked: the top of the valence band remains located in Γ and no longer displays the flat feature in the SixOy superlattices (Figure 13). The bottom of the conduction band is defined by two minima lying close to each other at 0.10 [Si5C0.25] and 0.28 [Si7C0.5] eV. The lowest one corresponds to the signature of bulk SiC (Figure 29), while the other one to the bulk Si one. For thin superlattices (Si5C0.25), the application of the uniform compressive stress induced by the C atoms leads to an isotropic electron effective mass of ~0.2 me. Increasing the number of Si layers to 7, at a fixed C concentration (Si7C0.25), reduces the strain (Figure 18) and restores partially the anisotropy of the band, as shown with the fluctuations of the electron effective masses (from 0.2 to 0.4 me in Figure 30). This effect disappears when going from Si7C0.25 to Si7C0.5 with the increase of the C concentration (and hence of the stress) into the superlattice.

The impact on the valence band (hole effective mass) is different: for thin monolayers (Si5C0.25), the distribution of the hole effective mass and its anisotropy is similar to the bulk one. Increasing the silicon thickness and the C concentration leads to a reduction of the anisotropy along the YZ and XZ planes while in the Si one (XY), it increases it.

For the Ge/GeC models, the stress imposed by the insertion of the carbon atoms leads to a closure of the band gap, independently of the concentration and of the number of germanium considered (up to 7ML) (Figure 18).

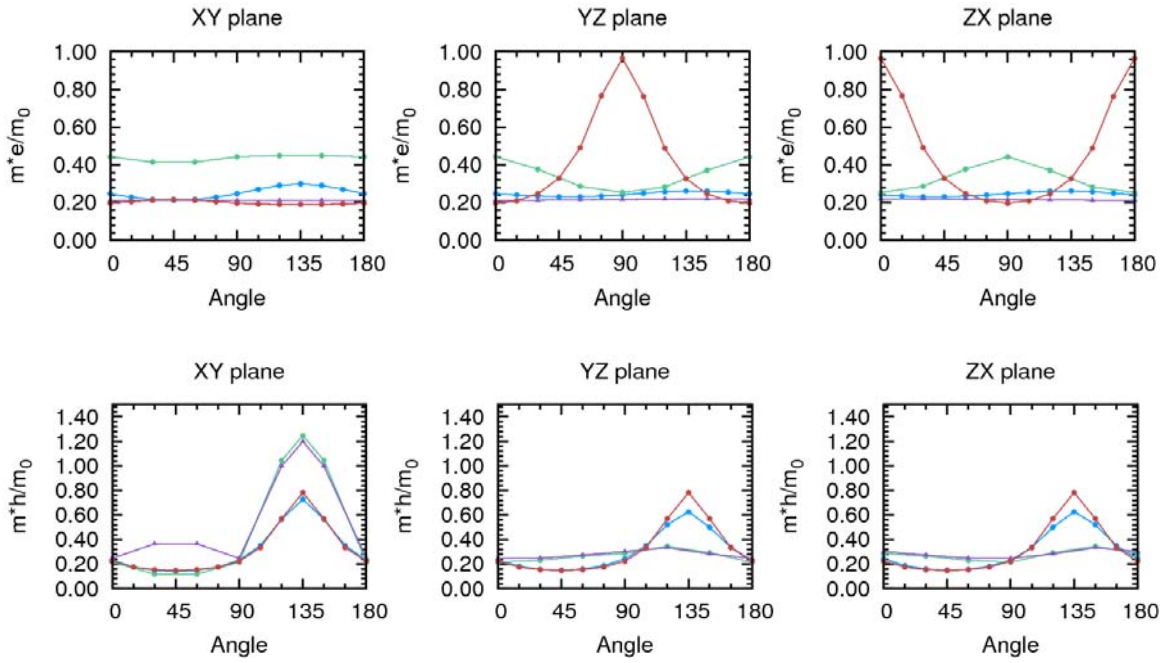

Figure 30: Electron (me) and hole (mh) effective masses computed in the XY, YZ and XZ planes (the plane of the Si monolayers is the XY one), starting from the X to Y, Y to Z and X to Z directions in the k space (Brillouin zone) computed for the top of the valence (top) and the bottom of the conduction bands (bottom) for the non-metallic Si5C0.25 (blue), Si7C0.25 (green), Si7C0.5 (purple) models and bulk silicon (red). The carbon layer is placed perpendicular to the Si plane (along the Z axis).

1.4 Conclusions

By using a combination of reactive molecular dynamics simulations and first-principles ones, we studied the structural and the electronic properties of Si(Ge)/O(C,N) superlattices accounting for different periodicities. The molecular dynamics simulations suggest, consistently with the experimental observations reported for the oxidation of Si in deliverable 3.3, that at room temperature, the reactions with the substrate with nitrogen and oxygen can be confined to the first 5 Å below the surface, allowing a (sub-)monolayer deposition of O (N). It is also found that the largest population of one- and two times coordinated Si with both O and N occurs at low fluence and at room temperature. In these conditions, the population of one-time coordinated Si atoms is maximized for the (100) orientation with respect to other substrate ones.

Ideal superlattice models, whose periodicity varies from 3 to 12 ML, have been built on the Si-O/SiN surface topologies gathered through molecular dynamics. The Ge ones were

constructed by substituting the Si sites by Ge in the models. Their structural and electronic properties suggest that:

1. The growth of epitaxial periodic Si(Ge)/O superlattices is possible provided that Si(Ge) lies in oxidation stage +1 (0.5 ML of O) at its interface with O. The adoption of higher oxidation degrees accumulates a large strain into the layers, which will leads to the formation of misfit dislocation/defects.
2. The electronic gap of the Si/O superlattices is predicted to be close to the bulk Si one up for periods up to 8ML of Si. For the Ge/O ones, it is reduced to half of the Ge bulk value.
3. The inserted O sub-monolayers induces a symmetry breaking into the band structure and is detrimental for the electron and hole effective masses for the Si models. For Ge ones, the inclusion of O reduces the electron and hole effective masses and their anisotropy, as from 6ML of Ge. This suggests that the system will display an enhancement of its hole and electron mobilities.
4. N can be incorporated up to 0.25 ML into the epitaxial Si(Ge)/N surperlattices and acts as a p-type doping source. Combined to hydrogen, it generates a spread in the electronic gap and in the effective masses of the Si superlattices. Depending on the Si thickness considered, this can be beneficial for either the hole or the electron effective masses. The atomic relaxation bound to the introduction of H is however very large and is expected to favor the amorphization of the superlattice. The GeN ones remain metallic upon the insertion of H.
5. The inclusion of C in the substrate to build Si(Ge) epitaxial superlattices is possible up to 0.25 ML. The strain induced closes the gap for the Ge systems. For the Si one, it generates a spread in the electronic gap and in the effective masses, which leads to a reduction of the electron effective masses and to an increase of the hole ones in the planes parallel to the C sub-monolayers.

In conclusion, the structural and electronic properties suggest that the most promising (stable) epitaxial superlattices for a Si/Ge thickness up to 7ML, arise from the combination of sub-monolayers of O and C with Si and Ge. Among these, only the Ge ones show interesting properties, which a predicted enhanced electron and hole mobilities with respect to their bulk counterparts. Also, our simulations point towards a high sensibility of the electronic properties of the superlattices to the structure of the interface between Si/Ge with the interspersing element.

Given that these structures rely on the building of a highly strained interface between Si/Ge and O/C/N compared to bulk Si and Ge, they lie at the border of the maximum deformation that typically Si and Ge can cope before relaxing their lattices through a dislocation process. Hence, the application of an external source of stress, as currently used to boost the electron and hole mobilities in current Si CMOS technology, will only lead to the relaxation of the strain present into the superlattice through the generation of defects and misfit dislocations. Hence the modeling of the impact of an external source of stress on the electronic properties has not been performed due the pointless aspect of the task.

1.5 References

{1} A. C. T, van Duin.; A. Strachan, S. Stewman, Q. Zhang, X. Xu, W.A.J. Goddard III, J. Phys. Chem. A, Vol. 107, pp. 3803 (2003).

{2} F. de Brito Mota, J. F. Justo, and A. Fazzio, J. Appl. Phys., Vol. 86, pp. 1843 (1999).

{3} G. C. Abell, Phys. Rev. B, Vol. 31, pp. 6184 (1985).

{4} A.C.T. van Duin, S. Dasgupta, F. Lorant, W.A. Goddart III, J. Phys. Chem. A, Vol. 105, pp. 9396; (2001).

{5} F. de Brito Mota, J. F. Justo, and A. Fazzio, J. Appl. Phys., Vol. 86, pp. 1843 (1999).

{6} G. Bussi, D. Donadio, M. Parinello, J. Chem. Phys., Vol. 126, pp. 014101 (2007).

{7} P. Giannozzi, S. Baroni, N. Bonini, M. Calandra, R. Car, C. Cavazzoni, D. Ceresoli, G. L. Chiarotti, M. Cococcioni, I. Dabo, A. Dal Corso, S. Fabris, G. Fratesi, S. de Gironcoli, R. Gebauer, U. Gerstmann, C. Gougoussis, A. Kokalj, M. Lazzeri, L. Martin-Samos, N. Marzari, F. Mauri, R. Mazzarello, S. Paolini, A. Pasquarello, L. Paulatto, C. Sbraccia, S. Scandolo, G. Sclauzero, A. P. Seitsonen, A. Smogunov, P. Umari, R. M. Wentzcovitch, J. Phys. Condens. Matter, Vol. 21, pp.395502 (2009).

{8} J. P. Perdew, K. Burke, and M. Ernzerhof, Phys. Rev. Lett., Vol. 77, pp. 3865 (1996).

{9} J. Heyd, G.E. Scuseria, and M., J. Chem. Phys. Vol. 118, pp. 8207 (2003).

{10} A. Alkauskas, P. Broqvist, and A. Pasquarello, Phys. Status Solidi B, Vol. 248, pp. 775 (2011).

{11} F. Tran and P. Blaha, Phys. Rev. Lett, Vol. 102, pp. 226401 (2009).

{12} V. I. Anisimov, F. Aryasetiawan and A. I. Lichtenstein, J. Phys.: Condens. Matter, Vol 9, pp. 767 (1997).

{13} C. H, Choi, D. Liu, J.W. Evans, M.S. Gordon, J. Am. Chem. Soc., Vol. 124, pp. 8730 (2002).

{14} J. H. Oh, K. Nakamura, K. Ono, M. Oshima, N. Hirashita, M. Niwa, A. Toriumi, A.J. Kakizaki, Elec. Spec. and Rel. Phen. Vol. 114, pp. 395 (2001).

{15} Y. Tu, Tersoff, J. Phys. Rev. Lett.,Vol. 84, pp. 4393 (2000).

{16} A. R. Khan, J. Stangl, G. Bauer, D. Buca, B. Holländer, H. Trinkaus, S. Mantl, R. Loo and M. Caymax, Semiconductor Science and Technology, Vol. 22, pp. S212 (2007).

{17} N. Xu, N. Damrongplasit, H. Takeuchi, R.J. Stephenson, N.W. Cody, A. Yiptong, X. Huang, M. Hytha, R.J. Mears and Tsu-Jae King Liu, IEEE International Electron Devices Meeting, San Francisco, USA, 2012, pp. 127.

{18} R. Tsu, J. C. Lofgren, J. Crystal Growth, Volumes 227–228, pp. 21-26 (2001).

{19} M. W. Haverkort, I. S. Elfimov, G. A. Sawatzky, http://arxiv.org/abs/1109.4036v1.

{20} H. N. Waltenburg, J. T. Yates, Chem. Rev. Vol. 95, pp. 1589 (1995).

{21} E. Horvath-Bordon, R. Riedel, A. Zerr, P. F. McMillan, G. Auffermann, Y. Prots, W. Bronger, R.D. Kniep and P. Kroll, Chem. Soc. Rev., Vol. 35, pp. 987 (2006).

{22} S. Madapura, A. J. Steckl, and M. Loboda , J. Elect. Soc., Vol. 146 (3) pp. 1197 (1999).

{23} H. Matsunami, Japanese J. App. Phys., Vol. 43, No. 10, pp. 6835 (2004).